Article

Cell Reports

Identification of an Early Unipotent Neutrophil Progenitor with Pro-tumoral Activity in Mouse and Human Bone Marrow

Graphical Abstract

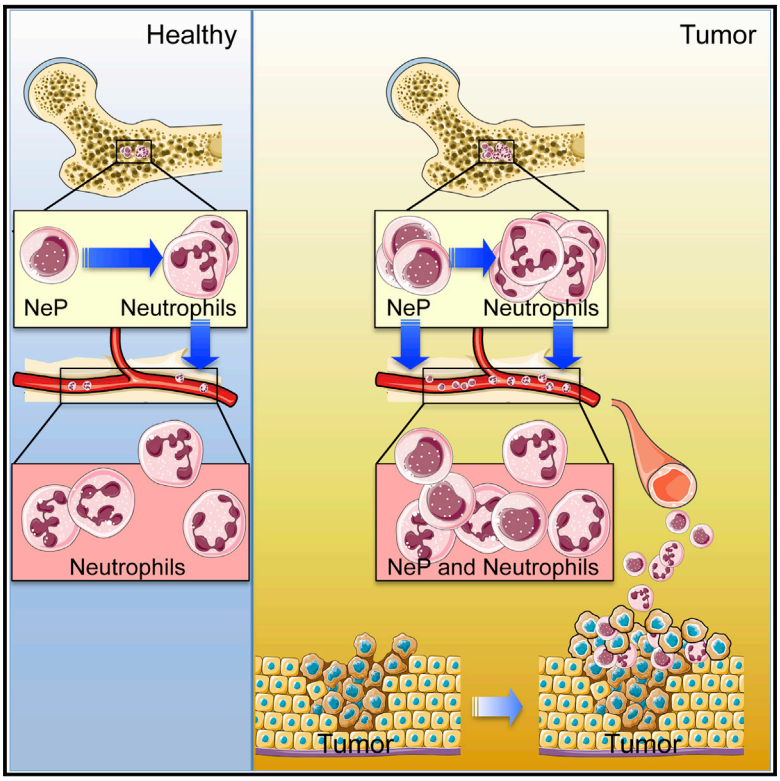

Highlights

- High-dimensional analysis of human bone marrow reveals neutrophil progenitor (NeP)
- NeP is unipotent and produces only neutrophils *in vivo*
- NeP suppresses T cell activation and promotes tumor growth in mouse models *in vivo*
- NeP expands in blood of humans with melanoma and in tumor-bearing mice

Authors

Yanfang Peipei Zhu, Lindsey Padgett, Huy Q. Dinh, ..., Ariel Madrigal, Pandurangan Vijayanand, Catherine C. Hedrick

Correspondence

peipei@lji.org (Y.P.Z.), hedrick@lji.org (C.C.H.)

In Brief

Zhu et al. discover an early unipotent neutrophil progenitor (NeP) in mouse and human bone marrow using high-dimensional profiling. NeP expand in cancer, suppress T cells, and promote tumor growth *in vivo*. NeP is found in the blood of human melanoma patients, suggesting that NeP could be a new cancer biomarker.

Zhu et al., 2018, Cell Reports *24*, 2329–2341
August 28, 2018
https://doi.org/10.1016/j.celrep.2018.07.097

CellPress

Cell Reports
Article

Identification of an Early Unipotent Neutrophil Progenitor with Pro-tumoral Activity in Mouse and Human Bone Marrow

Yanfang Peipei Zhu,[1,*] Lindsey Padgett,[1] Huy Q. Dinh,[1] Paola Marcovecchio,[1] Amy Blatchley,[1] Runpei Wu,[1] Erik Ehinger,[1] Cheryl Kim,[2] Zbigniew Mikulski,[1] Gregory Seumois,[3] Ariel Madrigal,[3] Pandurangan Vijayanand,[3] and Catherine C. Hedrick[1,4,*]

[1]Division of Inflammation Biology, La Jolla Institute for Allergy and Immunology, La Jolla, CA 92037, USA
[2]Flow Cytometry Core Facility, La Jolla Institute for Allergy and Immunology, La Jolla, CA 92037, USA
[3]Division of Vaccine Discovery, La Jolla Institute for Allergy and Immunology, La Jolla, CA 92037, USA
[4]Lead Contact
*Correspondence: peipei@lji.org (Y.P.Z.), hedrick@lji.org (C.C.H.)
https://doi.org/10.1016/j.celrep.2018.07.097

SUMMARY

Neutrophils are short-lived cells that play important roles in both health and disease. Neutrophils and monocytes originate from the granulocyte monocyte progenitor (GMP) in bone marrow; however, unipotent neutrophil progenitors are not well defined. Here, we use cytometry by time of flight (CyTOF) and single-cell RNA sequencing (scRNA-seq) methodologies to identify a committed unipotent early-stage neutrophil progenitor (NeP) in adult mouse bone marrow. Importantly, we found a similar unipotent NeP (hNeP) in human bone marrow. Both NeP and hNeP generate only neutrophils. NeP and hNeP both significantly increase tumor growth when transferred into murine cancer models, including a humanized mouse model. hNeP are present in the blood of treatment-naive melanoma patients but not of healthy subjects. hNeP can be readily identified by flow cytometry and could be used as a biomarker for early cancer discovery. Understanding the biology of hNeP should allow the development of new therapeutic targets for neutrophil-related diseases, including cancer.

INTRODUCTION

Neutrophils are the most abundant population of circulating blood leukocytes. With many emerging studies suggesting critical roles of neutrophils in chronic inflammatory diseases, including cancer, a complete understanding of neutrophil development is imperative (Huang et al., 2016; Sagiv et al., 2015; Soehnlein et al., 2017; Summers et al., 2010). Neutrophils originate in the bone marrow (BM). In murine BM, $Lin^{-}CD117$ (c-kit)$^{+}$ (LK) cells include $Lin^{-}CD117^{+}Ly6A/E$ (Sca1)$^{+}CD127^{-}$ (LSK) cells that give rise to all hematopoietic cells, $Lin^{-}CD117^{lo}Ly6A/E^{+}CD127^{+}$ cells that contain the common lymphoid progenitor (CLP) that give rise to all lymphoid lineages, and Lin^{-} $CD117^{+}Ly6A/E^{-}$ that selectively generate only myeloid lineages (Akashi et al., 2000). In this classic hematopoietic paradigm, the Lin^{-} $CD117^{+}$ $Ly6A/E^{-}$ population is divided into common myeloid progenitor (CMP), megakaryocyte-erythroid progenitor (MEP), and granulocyte monocyte progenitor (GMP) by differential expression of surface markers CD16/32 (FcRγIII/II) and CD34 (Akashi et al., 2000). CMPs are the multipotent progenitors for MEP and GMP, whereas GMP have lost erythroid potency and thus are restricted to generate granulocyte and monocyte lineages (Manz et al., 2002).

High-dimensional mass cytometry (also known as cytometry by time of flight [CyTOF]) has become a powerful tool to investigate the hematopoietic system (Becher et al., 2014; Bendall et al., 2011; Samusik et al., 2016). Notably, with the development of multi-channel flow cytometry, mass cytometry and single-cell RNA sequencing (scRNA-seq), new markers have allowed the discovery of several new hematopoietic progenitors, including a $CD41^{+}$ megakaryocyte progenitor (MkP), a $Ter119^{+}$ erythroid precursor (Pro Ery) (Pronk et al., 2007), and the $Ly6C^{+}$ committed monocyte progenitor (cMoP) (Hettinger et al., 2013). The heterogeneity of GMP has been suggested in many studies. In mouse, single-cell analysis of gene expression patterns revealed that GMP already have restricted lineage potential toward monocytes or neutrophils (Buenrostro et al., 2018; Olsson et al., 2016). Gene expression analysis of CMP and GMP at the single-cell level showed heterogeneity in these progenitors (Paul et al., 2015), suggesting that classification of these subsets using solely CD34 and CD16/32 was not sufficient. In agreement with gene expression analysis, additional heterogeneity has been discovered in Lin^{-} $CD117^{+}$ $Ly6A/E^{-}$ cells with the use of additional surface markers. For example, CD105, CD150, CD41, and CD71 divide Lin^{-} $CD117^{+}$ $Ly6A/E^{-}$ cells into pre-MegE, preCFU-E, CFU-E, MkP, preGM, GMP, and Pro Ery (Pronk et al., 2007). $CX3CR1^{+}$ $CD115^{+}$ $CD135^{+}$ monocyte/DC progenitors (MDP) were also found to partially overlap with the classic CMP/GMP (Auffray et al., 2009). GMP heterogeneity has also been suggested in humans (Buenrostro et al., 2018) with similar developmental-staged transcriptional factors (such as IRF8) in mouse (Olsson et al., 2016). Comparable with GMP, myeloblasts are known to have both granulocytic and monocytic potentials (Borregaard, 2010). The use of CD64 identified a

human CD34^{+}CD64^{hi} monocyte progenitor within human GMPs (Kawamura et al., 2017).

In mouse, several monocyte progenitors (Fogg et al., 2006; Hettinger et al., 2013; Liu et al., 2009; Satoh et al., 2017) and granulocyte progenitors, including eosinophil progenitors (Mori et al., 2009; Zhang et al., 2004) and basophil/mast cell progenitors (Arinobu et al., 2005; Qi et al., 2013), have been identified. Several immature neutrophil precursors have also been identified (Fiedler and Brunner, 2012; Kim et al., 2017; Satake et al., 2012; Sturge et al., 2015; Yáñez et al., 2015). However, these precursors are late-stage precursors with neutrophil potency (Kim et al., 2017; Sturge et al., 2015), and several show multi- or oligo-potency (Satake et al., 2012; Yáñez et al., 2015). Recently, a proliferative neutrophil precursor was identified in mouse BM that generates neutrophils after intra-BM adoptive transfer (Evrard et al., 2018). However, the long-term potency of this precursor was not tested. Thus, several gaps in understanding the complete neutrophil-lineage hierarchy from CMP to mature neutrophils remain.

In humans, the search for a unipotent neutrophil progenitor (hNeP) has been ongoing for decades (Bainton et al., 1971; Elghetany et al., 2004; Pillay et al., 2010; Terstappen and Loken, 1990). Human CMP and GMP express positive levels of CD34 and CD38 and mirror the murine CMP/GMP paradigm in myeloid cell production (Doulatov et al., 2010; Edvardsson et al., 2006; Manz et al., 2002). A missing link in human neutrophil development is the identification of NePs that are downstream of GMP but upstream of short-term neutrophil precursors. Recently, mass cytometry analysis of human BM neutrophils indicates that human neutrophils are heterogeneous and contain a CD117^{-}CD34^{-}CD49d^{+}CD101^{-} subset termed preNeu (Evrard et al., 2018). This subset was suggested to be a counterpart of mouse neutrophil precursors, but unfortunately the neutrophil potential of this possible precursor was not evaluated.

Here, we decided to take advantage of mass cytometry and viSNE (visualization of t-distributed stochastic neighbor embedding) automated mapping to identify and study new NePs in mouse and human BM.

RESULTS

Automated Single-Cell Analysis of Lin^{-} CD117^{+} Ly6A/E^{-} Cells Identifies a Distinct NeP Population

We analyzed mouse BM using mass cytometry with the purpose of identifying all NePs. We developed an antibody panel, shown in Table S1, that measures 39 parameters simultaneously and used it to perform CyTOF mass cytometry on healthy mouse BM. We used viSNE automated analysis to study CD45^{+} BM cells and found a portion of CD117(c-Kit)$^{+}$ cells that had close relation to Ly6G^{+} cells (Figure S1A). Interestingly, CD34^{+} GMP clustered with different populations, including the Ly6G-enriched population and the CD115-enriched population (Figure S1B). These results agree with the reported observation that CD115^{+} MDP overlaps with CMP/GMP (Auffray et al., 2009) and, more important, suggest that the GMP fraction has NeP potential. We then focused exclusively on myeloid cells by examining the Lin^{-} CD117^{+} Ly6A/E^{-} fraction of LK cells, which contains all myeloid cell progenitors (Figure S1C). Using viSNE automated unbiased analysis, we found five distinct clusters of cells in Lin^{-} CD117^{+} Ly6A/E^{-} cells, which we labeled as clusters #A–#E in Figure 1A. Each of these clusters expresses distinctive biomarkers that uniquely define specific myeloid cell types. Siglec F (cluster #A) marks eosinophils, CD115 (cluster #B) marks monocytes, Ly6G (cluster #C) marks neutrophils, FcεRIα (cluster #D) marks mast cells and basophils, and CD16/32 and CD34 (cluster #E) marks both CMP and GMP. The neutrophil-specific antigen, Ly6G, is observed in a continuum from negative to high expression in cluster #C, suggesting the presence of NeP and precursors within this cluster (Kim et al., 2017; Satake et al., 2012; Sturge et al., 2015; Yáñez et al., 2015). We confirmed these results using conventional flow cytometry (Figures S2A and S2B).

Because we were interested in identifying NePs, we focused our efforts on further analysis of cluster #C, which showed a continuum of Ly6G expression. Using PhenoGraph, a second unbiased clustering algorithm (Chen et al., 2016; Levine et al., 2015), we found that cluster #C consists of two major populations that display a continuum of Ly6G, Ly6C, and Ly6B expression (Figure 1B). These Ly6 proteins are highly expressed in mature neutrophils and their precursors (Kim et al., 2017; Lee et al., 2013). We developed a conventional flow cytometry gating strategy, shown in Figure 1C, to isolate with purity cluster #C cells (Lin^{-} CD117^{+} Ly6A/E^{-} Siglec F^{-} FcεRIα^{-} CD16/32^{+} Ly6B^{+} CD162^{lo} CD48^{lo} Ly6C^{lo} CD115^{-}) from BM. This cell population, when backgated onto a viSNE map, fell exclusively into cluster #C (Figure 1C).

ScRNA-Seq Analysis of Cluster #C Reveals Two Major Subpopulations, #C1 and #C2

To closely investigate cluster #C, we sorted cluster #C cells for scRNA-seq. We found two primary subpopulations within cluster #C, #C1 and #C2 (Figure 2A), by scRNA-seq. Notably, #C1 shows low *Ly6g* expression at the mRNA level (Figure 2A), which confirms our low Ly6G protein expression in this cluster found by mass cytometry (Figure 1B).

Using these data, we were able to design a flow cytometry panel (Figure 2B) that allowed us to isolate both #C1 and #C2 as well as other Lin^{-} CD117^{+} Ly6A/E^{-} cell fractions for further detailed study. Cluster #C1 is Lin^{-} CD117^{+} Ly6A/E^{-} Siglec F^{-} FcεRIα^{-} CD16/32^{+} Ly6B^{+} CD11a^{+} (LFA1α^{+}) CD162^{lo} CD48^{lo} Ly6C^{lo} CD115^{-} Ly6G^{-}, and cluster #C2 is Lin^{-}CD117^{+} Ly6A/E^{-} Siglec F^{-} FcεRIα^{-} CD16/32^{+} Ly6B^{+} CD11a^{+} (LFA1α^{+}) Ly6G^{+}. On the basis of surface marker expression patterns, we predict #C1 and #C2 as NeP candidates.

As identified in Figure 1A, cluster #E is enriched with CD16/32^{-}CD34^{+} CMPs, and cluster #B is enriched with CD115^{+} monocyte progenitors. We performed bulk RNA-seq for transcriptome analysis on #C1 and #C2 and analyzed #E and #B cells as control groups. BM neutrophils (BM Neuts) containing immature and mature neutrophils were also sorted from the same donors for analysis. We found that #C1 expresses high levels of GMP genes, including *Egr1*, *Fosb*, *Jun*, *Gata2*, and *Gata1*, as well as genes that are shown to be critical for neutrophil development, including *Gfi1*, *Cebpa*, *Cebpe*, *Per3*, and *Ets1* (Avellino et al., 2016; Buenrostro et al., 2018; Evrard et al., 2018; Horman et al., 2009; Olsson et al., 2016; Radomska et al., 1998; Zhang

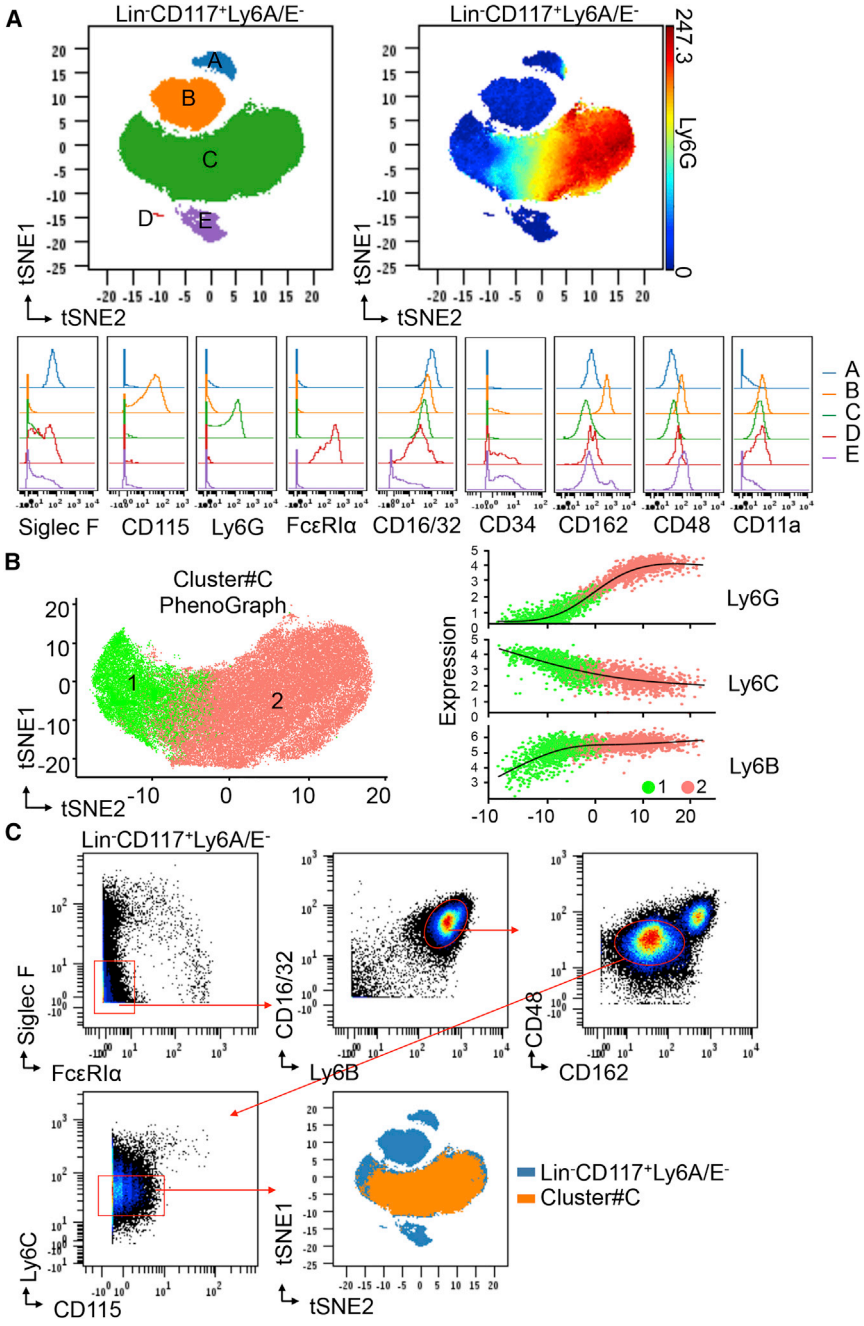

Figure 1. Automated Single-Cell Analysis of Lin⁻ CD117⁺ Ly6A/E⁻ Cells in Bone Marrow Identifies a Distinct Neutrophil Progenitor Population

(A) ViSNE defines a largest cluster #C of the five subsets in Lin⁻ CD117⁺ Ly6A/E⁻ cells from murine BM using mass cytometry (CyTOF). BM cells isolated from C57BL/6J donors were stained with the antibody panel shown in Table S1. ViSNE maps of Lin⁻ CD117⁺ Ly6A/E⁻ cells are shown as dot overlays to display the five automated clusters (#A–#E). Ly6G expression pattern is shown on viSNE map of Lin⁻ CD117⁺ Ly6A/E⁻ cells as spectrum colored dots. The expression patterns of the indicated markers are shown as histogram overlays of each cluster. Results are representative of two independent experiments (n = 6 mice each). (See CyTOF panel in Table S1, CyTOF gating strategy in Figure S1, and flow cytometry gating strategy in Figure S2.)

(B) PhenoGraph defines two subpopulations of cluster #C using mass cytometry (CyTOF). Left: two PhenoGraph meta-clusters present two distinct populations (1, 2) in cluster #C. Right: expression profile of Ly6G, Ly6C, and Ly6B for randomly selected cells in each cluster is visualized on the first component of a nonlinear dimensionality reduction isomap (the regression black line estimated using the generalized linear model is added for each marker).

(C) FACS gating strategy for cluster #C using mass cytometry (CyTOF). Manually gated cluster #C is backgated to automated viSNE map for validation. (See flow cytometry gating strategy in Figure S2C.)

et al., 1997). Genes that are critical for monocyte development, such as *Irf8* (Olsson et al., 2016; Yáñez et al., 2015), on the other hand, show low expression in #C1 and #C2. Interestingly, #C2 cells have lost expression of the GMP gene signature, while the neutrophil gene signature increased in #C2 cells to levels comparable with those of BM Neuts.

We next wanted to focus on the hierarchical structure of #C1 and #C2 within the neutrophil developmental lineage. Frequencies of #C1 are lowest in BM, followed by #C2 (Figure S3A). Comparison of #C1 and #C2 by flow cytometry showed a gradient of Ly6G expression from negative in #C1 to intermediate in #C2 to high in mature BM Neuts, whereas CXCR2 is expressed only by terminally differentiated BM Neuts (Figure S3A). Reconstruction in three dimensions of the nuclear architecture of #C1 and #C2 cells suggests more stem cell-like morphology than that of mature BM Neuts and blood neutrophils (blood Neuts) (Figure S3B). #C1 has more stem cell-like nuclear morphology and higher Ki67 expression and nuclear integration (Figures 2C and S3C) than does #C2, BM Neuts, and blood Neuts, suggesting an early stage of development for #C1. These data suggest that #C1 lies earlier in the neutrophil developmental hierarchy and may partially overlap with GMP from the classic myeloid progenitor paradigm. #C2, however, may represent a transitional intermediate progenitor between #C1 and terminally differentiated neutrophils in mouse BM. Thus, we then decided to focus on #C1 cells as the candidate for the early-stage committed NeP.

The selective neutrophil potency of #C1 cells was first tested by examining *in vitro* methylcellulose colony-forming unit formation (Figure 2E). All donor cell fractions were sorted using fluorescence-activated cell sorting (FACS) using the gating

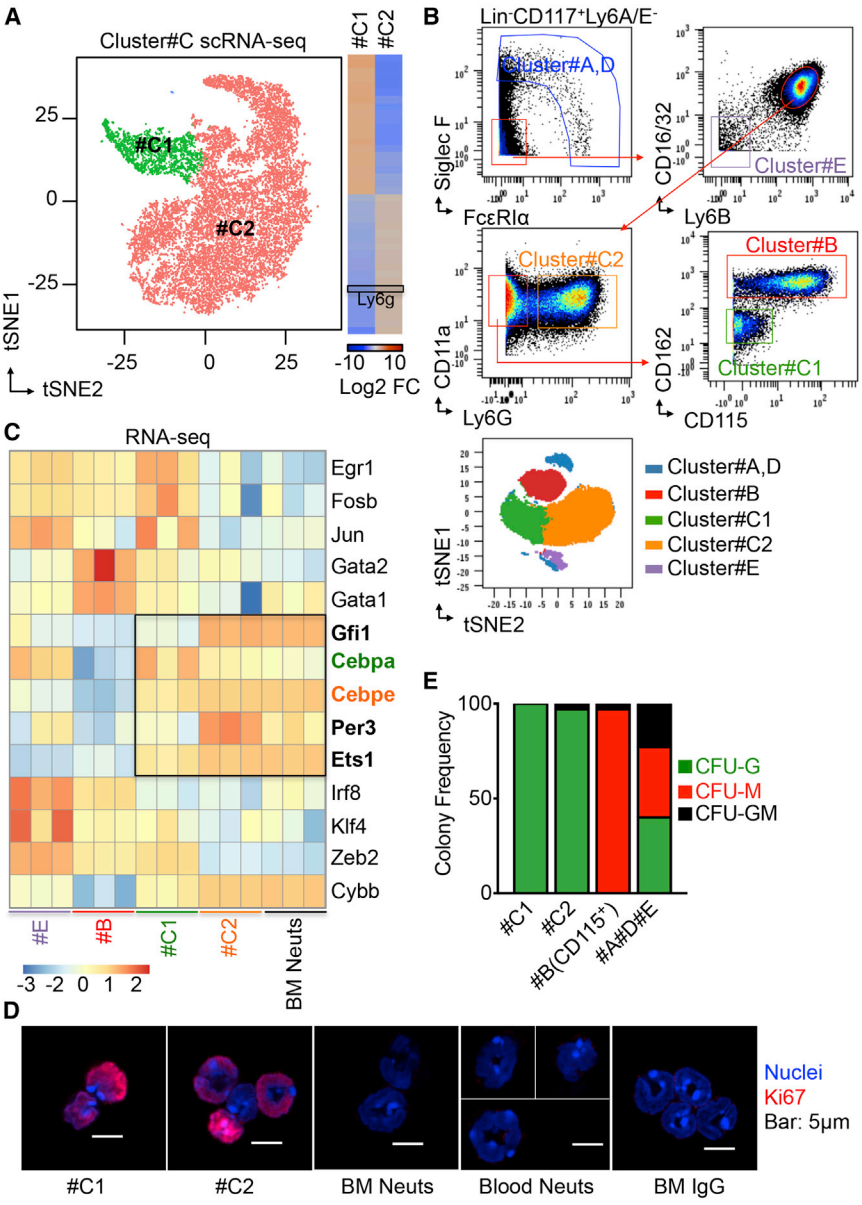

Figure 2. ScRNA-Seq Analysis of Cluster #C Reveals Two Major Subpopulations, #C1 and #C2

(A) Single-cell RNA sequencing (scRNA-seq) uncovers the heterogeneity of cluster #C. Twenty thousand cluster #C cells were sorted from healthy wild-type mouse BM for scRNA-seq assay (three biological triplicates, two technical replicates). FACS strategies for cluster #C are shown in Figure 1C using mass cytometry and Figure S2C using flow cytometry. Left: t-distributed stochastic neighbor embedding (t-SNE) two-dimensional (2D) plots, obtained applying Seurat scRNA-seq analysis R package for the scRNA-seq data, showing two main clusters corresponding to subsets of cluster #C (n = 16,268 cells; #C1, 2,149 cells [green]; #C2, 14,089 cells [salmon]). Right: heatmap shows top 40 differentially expressed genes in each cluster. Black box highlights Ly6G expression. Log_2 fold change of each gene expression is relative to the entire dataset.

(B) FACS gating strategy for clusters #A and #D, #B, #C1, #C2, and #E using mass cytometry (CyTOF). Manually gated clusters are backgated to automated viSNE map for validation. (See flow cytometry gating strategy in Figure S3D.)

(C) RNA-seq shows upregulation of important neutrophil lineage-decision genes in #C1 and #C2. Clusters #C1, #C2, and #E and BM Neuts were sorted from healthy wild-type mice BM for RNA-seq. FACS strategies for these cell types are shown in Figure 2B using mass cytometry and Figure S3D using flow cytometry. Heatmap showing expression of important development transcriptional factors for myeloid cell development in sorted populations by RNA-seq. Black box highlights expression of important neutrophil lineage-decision genes (bold) in #C1 and #C2. Cebpa (green) expression is higher in #C1 compared with #C2. Cebpe (orange) expression is lower in #C1 compared with #C2. *Z* score normalization from CPM (counts per million) expression level (log_2 scale) was quantified from RNA-seq.

(D) Confocal microscopy detected Ki67 localization within the nuclei in clusters #C1and #C2. #C1, #C2, BM Neuts, and blood Neuts were sorted and stained with antibodies to Ki67 (red), and DNA was labeled with Hoechst (blue). FACS strategies for these cell types are shown in Figure 2B using mass cytometry and Figure S3D using flow cytometry. IgG-stained cells served as a negative control. Scale bar, 5 μm.

(E) Clusters #C1 and #C2 cells produce only neutrophils *in vitro*. Clusters #C1, #C2, #B ($CD115^+$), #A, #D, and #E cells were sorted from wild-type mice and diluted to single-cell suspensions. FACS strategies for these cell types are shown in Figure 2B using mass cytometry and Figure S3D using flow cytometry. Single cells of each cluster were cultured in methylcellulose-based medium. Numbers of colonies generated from the indicated progenitors were counted at day 10 of culture. Contingency plot shows mean value of six independent experiments (each contains three biological triplicates). (See also Figure S3.)

strategy described in Figure 2B. $CD115^+$ $CD117^+$ cells are monocyte progenitors and are located within cluster #B, so the $CD115^+$ portion of cluster #B was sorted as monocyte progenitors (Figure S4A). Clusters #A, #D, and #E were collected together as a control group. As shown in Figure 2E, #C1 single cells generate colony-forming unit-granulocyte (CFU-G) in methylcellulose-based medium with 100% purity, but not colony-forming unit-macrophage (CFU-M) or colony-forming unit-granulocyte, macrophage (CFU-GM). Similar results were also observed with #C2. Cluster #B ($CD115^+$) cells were able to generate CFU-M only, as expected. The #A#D#E control group generated all three types of colonies. These results suggest that #C1 cells have restricted granulocyte potency *in vitro* that lasts at least 10 days.

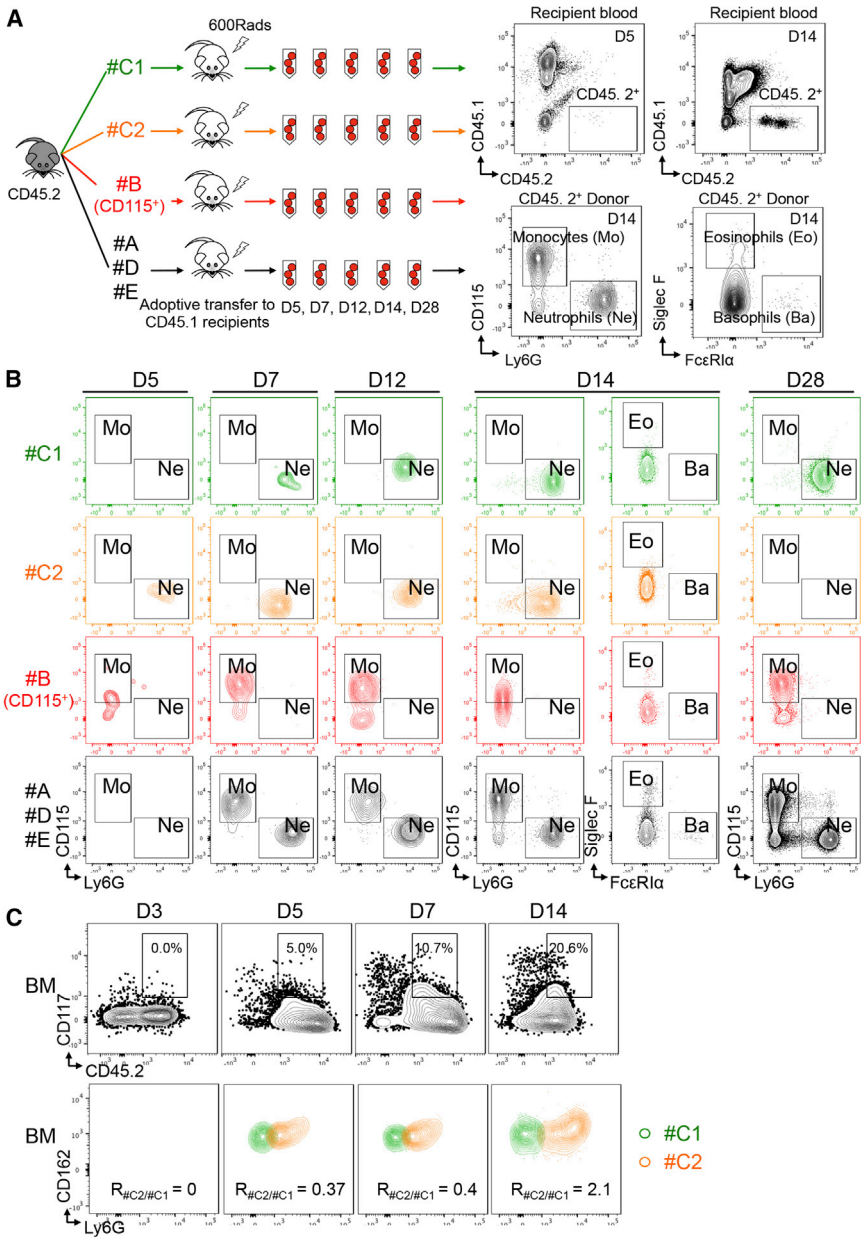

Figure 3. Clusters #C1 and #C2 Cells Are Committed Hierarchical Unipotent Progenitors for Neutrophil Production *In Vivo*

(A) Scheme showing the experimental procedure. Clusters #C1 and #C2 were sorted from CD45.2 donors and adoptively transferred into irradiated wild-type CD45.1 recipient mice. Clusters #B (CD115$^+$), #A, #D, and #E cells were sorted from the same donors for this experiment and served as controls. FACS strategies for these cell types are shown in Figure 2B using mass cytometry and Figure S3D using flow cytometry. Each recipient group includes 25 mice. Each recipient received 50,000 donor cells. After the transfer, peripheral blood was collected for flow cytometry of CD45.2$^+$ cells from five recipients of each group at days (D) 5, 7, 12, 14, and 28. CD45.2$^+$ cells were evaluated for the donor cell-derived monocytes (CD115$^+$), neutrophils (Ly6G$^+$), eosinophils (Siglec F$^+$), and basophils (FcεRIα$^+$). N = 5 mice for each time point in each group. (See FACS strategy in Figures S3D and S4A.)

(B) Clusters #C1 and #C2 cells produce only neutrophils *in vivo*. Representative plots show the appearance of neutrophils and monocytes in each recipient group at the time points indicated. Results are representative of two independent experiments. (See quantification in Figure S4.)

(C) Cluster #C1 produces #C2 cells *in vivo*. #C1 cells were sorted from CD45.2 donors and adoptively transferred into irradiated wild-type CD45.1 recipient mice. FACS strategies for #C1 cells are shown in Figure 2B using mass cytometry and Figure S3D using flow cytometry. After transfer, BM was collected for flow cytometry of CD45.2$^+$ cells from three recipients of each group at days (D) 3, 5, 7, and 14. CD117$^+$CD45.2$^+$ cells were evaluated for the donor #C1 homing to bone marrow and differentiation into #C2 cells. Expression in recipients of #C1 and #C2 cells are identified by the panel shown in Figures 2B and S3D and overlaid for display. #C2 differentiation into #C2 cells are shown as the ratio of #C2 to #C1 ($R_{\#C2/\#C1}$). (See also Figure S4.)

Cluster #C1 Is the Early-Stage Committed Unipotent NeP *In Vivo*

We next analyzed the function of #C1 in generating neutrophils *in vivo* using adoptive transfer approaches. The experimental scheme is shown in Figure 3A. The cell populations described in Figure 2E were FACS-sorted from the same donor mice. Each of the four cell groups was adoptively transferred into a group of sub-lethally irradiated CD45.1 recipient mice. Blood from each group was examined at days 5, 7, 12, 14, and 28 by flow cytometry for appearance of donor-derived progeny. The flow cytometry gating for all donor cell progeny is shown in representative plots of the #A#D#E recipient group in Figure 3A (right). Donor cells (CD45.2$^+$) appeared in blood as early as day 5 and peaked at day 14 (Figure 3A, right, and Figure S4B, left). Donor cells were analyzed for expression of key markers for myeloid progenies: monocytes (Mo, CD115$^+$), neutrophils (Ne, Ly6G$^+$), eosinophils (Eo, Siglec F$^+$), or basophils (Ba, FcεRIα$^+$).

Donor-derived neutrophils appeared in recipient blood at day 5 and day 7 post-adoptive transfer in the groups reconstituted with #C1 (green) and #C2 (orange), suggesting neutrophil potency in both populations and slower kinetics of the #C1 cells in producing neutrophils (Figure 3B). NePs from these progenitors constitute nearly 100% of CD45.2$^+$ donor cell-derived leukocytes in the #C1 recipients (Figure S4B, middle). In the control groups, #B (CD115$^+$) produced only monocytes and did not produce neutrophils, and #A#D#E produced both neutrophils and monocytes (Figures 3B and S4B, red and black). These results illustrate the restricted

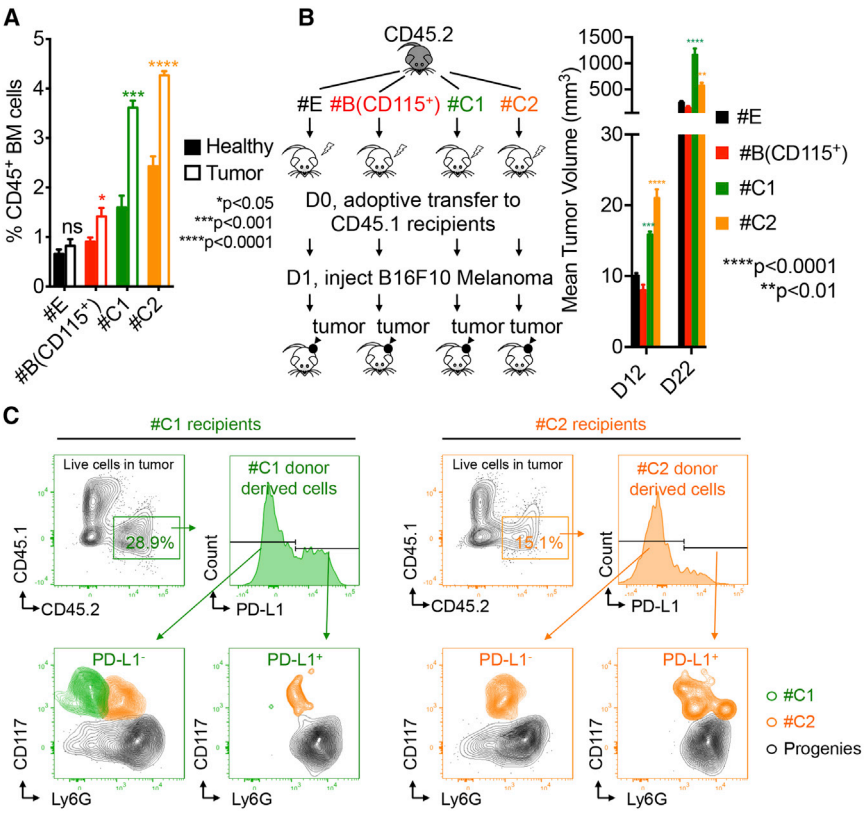

Figure 4. Cluster #C1 NeP and #C2 Cells Are Increased in BM with Tumor and Promote Tumor Growth *In Vivo*

(A) Cluster #C1 NeP and #C2 cells are increased in BM of tumor-bearing mice. Five hundred thousand B16F10 melanoma cells were s.c. injected into the rear flank of wild-type recipient mice for primary tumor growth. The frequencies of clusters #E, #B (CD115$^+$), #C1, and #C2 were detected in BM from tumor-bearing mice at 14 days post-injection (open bars) or their healthy counterparts (solid bars). N = 15. Error bars indicate mean (SD). (See also Figure S5.)

(B) Left: scheme showing the experiment procedure. Clusters #E, #B (CD115$^+$), #C1, and #C2 were sorted from the same CD45.2 wild-type donors and were adoptively transferred into sublethally irradiated congenic CD45.1 recipients. FACS strategies for these cell types are shown in Figure 2B using mass cytometry and Figure S3D using flow cytometry. Each recipient received 5×10^4 donor cells. The next day, 3×10^5 B16F10 melanoma cancer cells were s.c. injected into each recipient mouse. Right: the tumor volume in each recipient was measured at 12 and 22 days post-injection. Results are representative of two independent experiments. N = 5 mice in each group. Error bars indicate mean (SD).

(C) Clusters #C1 and #C2 cells infiltrate to tumor and generate PD-L1-positive progenies. At day 22 (D22) after the adoptive transfer, the tumors were harvested from recipients. Live singlet cells in tumor were evaluated using flow cytometry. CD45$^+$ donor-derived cells were analyzed for PD-L1 expression. #C1, #C2, and donor-derived neutrophils were identified with the panel from Figures 2B and S3D and overlaid for display. (See also Figure S5.)

unipotency of #C1 and #C2 progenitors to generate solely neutrophils.

Neutrophil production peaks at day 14 in #C2 recipients, but at day 28, neutrophils vanished from the #C2 recipients, suggesting limited developmental potency of #C2 (Figure S4B, right). However, in #C1 recipients, neutrophil production continued to day 28, our latest time point, indicating that the #C1 progenitors have longer term potency. This long-term potency of #C1 is comparable with the #A#D#E fractions of Lin$^-$ CD117$^+$ Ly6A/E$^-$ cells, which contains CMP. To further determine that #C1 cells give rise to #C2 cells, we FACS-sorted only the #C1 cells (using the gating strategy shown in Figure 2B) from CD45.2 BM and adoptively transferred these CD45.2$^+$ #C1 cells into CD45.1 recipients. We tracked the fate of the CD45.2$^+$ #C1 donor cells by examine the recipients' peripheral and BM for the production of #C2 after the adoptive transfer. As shown in Figures 3C and S4C (top), #C1 cells infiltrated into spleen quickly by day 3 and appeared in BM 5 days after adoptive transfer. Importantly, a portion of the CD45$^+$ #C1 donor cells started to generate #C2 very quickly after adoptive transfer, while some #C1 cells seeded in the BM (Figures S4C and 3C, bottom), again confirming that #C1 is the early-stage committed NeP.

Thus, by using high-dimensional mass cytometry and scRNA-seq approaches, as well as adoptive transfers *in vivo*, we have discovered an early-stage committed unipotent NeP (#C1, termed NeP) in mouse BM. This progenitor can be identified as Lin$^-$ CD117$^+$ Ly6A/E$^-$ Siglec F$^-$ FcεRIα$^-$ CD16/32$^+$ Ly6B$^+$ CD11a$^+$ CD162^{lo} CD48^{lo} Ly6C^{lo} CD115$^-$ Ly6G$^-$.

Cluster #C1 Cells Are Increased in BM and in Periphery with Tumor and Promote Tumor Growth *In Vivo*

Granulopoiesis is associated with cancer, with neutrophils having both pro-tumoral and anti-tumoral roles (Casbon et al., 2015; Hagerling and Werb, 2016; Sagiv et al., 2015). We wondered what role #C1 NeP would have in tumorigenesis *in vivo*. We first asked whether #C1 or #C2 cells were increased in BM in a melanoma mouse model. We injected B16F10 tumor cells subcutaneously (s.c.) into the rear flank of wild-type C57BL/6J mice (tumor). Age- and gender-matched wild-type mice received D-PBS to serve as healthy controls (healthy). At 14 days post-injection, we found a significant expansion of #C1 NeP and #C2 cells and a slight increase of #B (CD115$^+$), but not #E (CMP) cells, in the BM of tumor-bearing mice (Figure 4A), indicating that in the setting of cancer, myelopoiesis is strongly geared toward the neutrophil lineage. Interestingly, we detected minimal numbers of cluster #C cells (less than 0.02% of all CD45$^+$ cells in the periphery) of healthy mice, whereas #C cells are increased 10-fold in periphery of tumor-bearing

mice (Figure S5A), suggesting that there is increased production and egress of these NePs from BM to periphery in response to the tumor microenvironment. To test whether NeP can directly contribute to tumor growth, #C1 NeP cells, #C2 cells, #B ($CD115^+$) cells, and #E cells were sorted from CD45.2 wild-type donor mice and adoptively transferred into irradiated CD45.1 recipient healthy mice. At day 1 after donor cell transfer, recipient mice were injected s.c. with B16F10 tumor cells into the rear flank. Tumor size was measured at days 12 and 22 after injection (Figure 4B, left). As shown in Figure 4B (right), mice receiving #C1 cells or #C2 cells showed increased tumor growth compared to #B ($CD115^+$) cells or #E cells (CMP) at both time points. #C1 NeP promoted more potent tumor growth at the later time point compared with #C2 cells. At day 22 after tumor injection, tumors were harvested for detection of donor-derived cells. More #C1 NeP-derived cells infiltrated the tumor than did #C2 cells, and more than 30% of these #C1 NeP-derived cells expressed PD-L1, an inhibitory costimulatory molecule that contributes to immune suppression (Figure 4C). Further analysis revealed that tumor-infiltrated #C1 cells were able to maintain their stem cell phenotype as well as produce PD-$L1^+$ #C2 and $CD117^-Ly6G^+$ neutrophils. #C2 cells were also able to promote tumor growth via the same mechanism but to a lesser degree, whereas other cell types did not infiltrate the tumor (#B) and showed minimal PD-L1 expression (#E) (Figure S5B). Thus, #C1 NeP progenitors respond to melanoma tumor cues and have tumor-promoting functions by producing immune-suppressive progenies.

Discovery of a Heterogeneous $CD66b^+CD117^+$ $CD38^+$ $CD34^{+/-}$ Progenitor-like Cell Fraction in Human BM

On the basis of our cancer findings in mice showing the relevance of NePs to tumor growth, we next decided to look for NePs in human BM. Human CMP and GMP express CD34, CD38, and CD117 and mirror the murine CMP/GMP paradigm in myeloid cell production (Doulatov et al., 2010; Edvardsson et al., 2006; Manz et al., 2002). CD66b is an important marker for neutrophil identification. However, it is often excluded from flow cytometry panels geared toward discovery of hematopoietic progenitors. We decided to retain this marker in our search for the early NeP in human BM. We developed a flow cytometry panel to investigate the neutrophil lineage by focusing on $CD45^+$ cells that excluded other hematopoietic stem/progenitor cells (HSPCs), including hematopoietic stem cells (HSC), multipotent progenitors (MPPs), CLP, multilymphoid progenitor (MLP), lymphoid-primed MPPs (LMPP), MEP, eosinophil progenitor (EoP), CMP, GMP, cMoP, and MDP and other terminally differentiated leukocytes (Doulatov et al., 2012; Edvardsson et al., 2006; Hoebeke et al., 2007; Kawamura et al., 2017; Kohn et al., 2012; Lee et al., 2015; Manz et al., 2002; Mori et al., 2009; Notta et al., 2016; Weiskopf et al., 2016). In this panel, all gates were strictly controlled with both single-color and fluorescence minus one (FMO) controls (Figure S6A). Indeed, we discovered that human BM contains a $CD66b^+$ population that expresses CD117 (Figure 5A), suggesting the presence of $CD66b^+$ stem cell progenitors within human BM (termed here as hNeP). This $CD66b^+CD117^+$ population expresses high levels of $CD38^+$ (Figure S6B), an important stem cell marker that is exclusively expressed by CMP/GMP (Doulatov et al., 2010, 2012; Kohn et al., 2012; Manz et al., 2002), suggesting that this population is committed to the myeloid lineage for development. ScRNA-seq analysis of this $CD66b^+CD117^+$ human NeP population revealed two major subsets that showed either positive (subset A) or negative (subset B) expression of CD34 (Figure 5B). Interestingly, lower CD34 gene expression in subset B is associated with increased expression of neutrophil-specific genes such as ELANE and LYZ (Figure 5B). We then confirmed the $CD34^+$ and $CD34^-$ subsets suggested by scRNA-seq by flow cytometry (Figure 6C). Both subsets appeared positive for Ki67 localization in the nuclei, suggesting active proliferation, with a slightly higher (about 1.3-fold) Ki67 mean fluorescence intensity value in $CD34^+$ hNeP compared with $CD34^-$ hNeP (Figure 5D).

Both hNeP Subsets Produce Only Neutrophils in NSG-SGM3 Mice

We then examined the neutrophil potency of both $CD34^+$ and $CD34^-$ hNeP subsets *in vivo* by performing adoptive transfers of each subset into NSG-SGM3 (NSG-M3) mice. The triple transgenic NSG-M3 mice are immunodeficient NOD scid gamma (NSG) mice that express the human cytokines interleukin-3 (IL-3), granulocyte/macrophage-stimulating factor (GM-CSF), and SCF, also known as KITLG. This mouse model supports stable engraftment of the human hematopoietic system, including the myeloid lineage (Billerbeck et al., 2011; Coughlan et al., 2016). The two subsets were isolated from fresh human BM by FACS using the sorting panel in Figure 5 and transferred into two groups of recipient NSG-M3 mice. Peripheral blood of each NSG-M3 recipient mouse was collected on days 5, 7, 14, and 28 for flow cytometry analysis (Figure 6A). To analyze the progeny produced, we used a control group of NSG-M3 recipient mice that received all $CD34^+$ HSPCs (which contain progenitors for all leukocyte cell types). The blood of this control group was analyzed for monocyte (Mo), neutrophils (Ne), eosinophils (Eo), and lymphocytes (Ly), including T cells, B cells, and natural killer (NK) cells using the flow cytometry panel shown in Figure S6C. This flow cytometry panel is then used for the analysis of hNeP recipient blood. After adoptive transfer, $CD66b^+$ cells were detected in both $CD34^+$ hNeP and $CD34^-$ hNeP recipients, but no other cell types were expressed (Figure 6B), illustrating that both hNeP subsets are unipotent progenitors that produce only neutrophils. Repopulation of the neutrophil pool by either hNeP progenitor subset occurred quickly after the adoptive transfer (day 5) and lasted to day 28 (Figure 6B), indicating relatively long-term neutrophil unipotency of both progenitor subsets. These data demonstrate that the $CD66b^+$ $CD117^+$ $CD38^+$ $CD34^{+/-}$ fraction in human BM cells contains the unipotent human NeP (hNeP) that occupies about 1%–3% of $CD45^+$ cells in human BM under homeostatic conditions.

hNeP Increase in Melanoma Patient Blood and Promote Early Osteosarcoma Tumor Growth in Humanized NSG-M3 Mice

We of course wanted to see if hNeP played a role in tumorigenesis. First, we analyzed blood from human subjects with melanoma for the presence of hNeP (Table S2). Flow cytometry analysis of blood from melanoma versus healthy patients blood using the panel in Figure 5 revealed the presence of

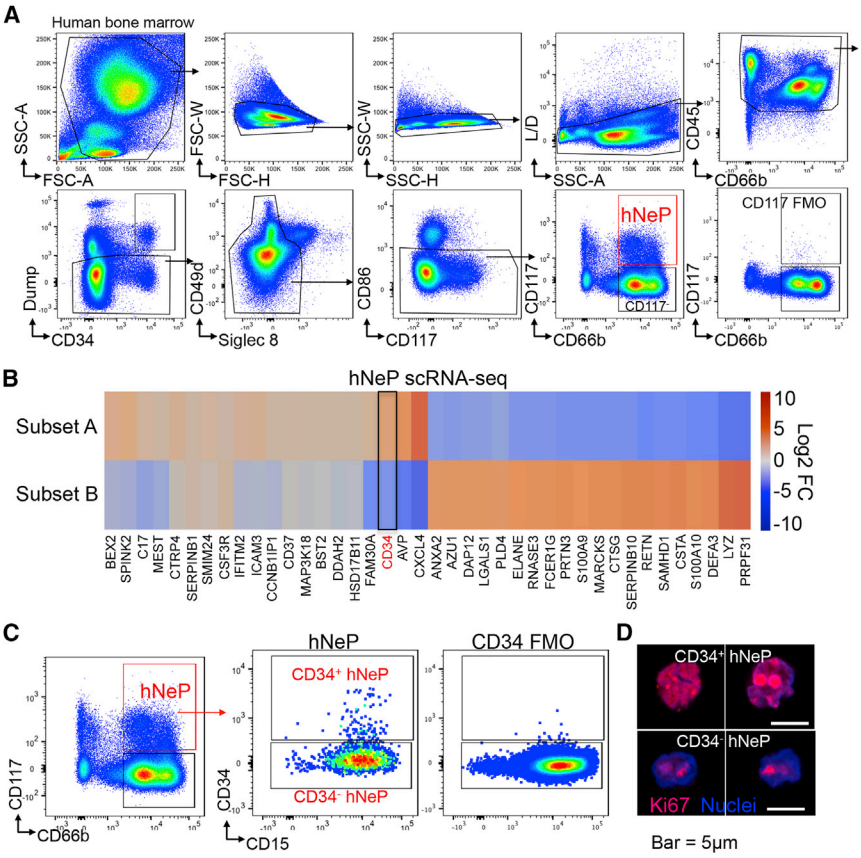

Figure 5. Human BM Contains a CD66b$^+$ CD117$^+$ hNeP Fraction that Contains CD34$^+$ and CD34$^-$ Subsets

(A) Flow cytometry analysis of healthy human BM uncovers a heterogeneous Lin$^-$CD66b$^+$CD117$^+$ hNeP fraction. Dump antibody cocktail contains antibodies against markers that are expressed by HSC (CD90 [Thy1]), lymphocytes and their progenitors (CD3, CD19, CD56, CD161, CD7, and CD127 [IL-7Rα]), erythrocytes and their progenitors (CD41 and CD235a [glycophorin A]), eosinophils/basophils and their progenitors (Siglec 8, FcεRIα, and CD125 [IL-5Rα]), CMP/GMP and monocyte progenitors (CD123 [IL-3Rα]), DCs, and macrophages (CD11c and CD169). (See also Figure S6.)

(B) ScRNA-seq analysis of Lin$^-$CD66b$^+$CD117$^+$ hNeP cells reveals two major subpopulations, subset A and subset B. Twenty thousand hNeP cells were FACS-sorted from healthy human BM for scRNA-seq. Heatmap shows top 40 differentially expressed genes in each cluster. Log_2 fold change of each gene expression is relative to the entire dataset. Two biological triplicates, two technical replicates.

(C) Lin$^-$CD66b$^+$CD117$^+$ hNeP were divided into CD34$^+$ subset and CD34$^-$ subset by flow cytometry. (D) Confocal microscopy was used to detect Ki67 localization (red) within the nuclei (blue) in CD34$^+$ subset and CD34$^-$ subset using antibodies to Ki67 and Hoechst. IgG-stained cells served as negative control. Scale bar, 5 μm.

CD66b$^+$CD117$^+$ cells (about 1% of circulating CD45$^+$ cells) in the blood of healthy donors (Figure 7A). The frequency of these hNeP was significantly elevated in the blood of melanoma patients, with frequencies of about 3%–9% of circulating CD45$^+$ cells (Figure 7A). We did not observe direct correlations between the hNeP frequencies and gender or age despite the small pool of donors (data not shown). Importantly, CD34$^+$ hNeP were barely detected in healthy donor blood but were elevated in the blood of melanoma patients (Figure 7A). This increase of hNeP cells in human melanoma patient blood is consistent with what we have observed for mouse NeP in our mouse melanoma model (Figure S5A), suggesting that the hNeP could serve as a biomarker candidate for early cancer detection.

Then we examined the role of hNeP in regulating multiple solid tumor types growth to see if the tumor-promoting role of NePs was relevant in more than one tumor type using NSG-M3 mice. A high neutrophil-to-lymphocyte ratio is an indicator of worse prognosis in sarcomas (Anderson, 2017). Here we used osteosarcoma as model of solid tumor. Shown in Figure 7B (left), both CD34$^+$ hNeP and CD34$^-$ hNeP were isolated from human BM and adoptively transferred into NSG-M3 recipient mice. Two different control groups were used in this experiment: one control group received only PBS for adoptive transfer, and the other group received human cMoP as a source of human monocyte progenitors. Human cMoP were sorted from the same human BM donor using the panel described previously (Kawamura et al., 2017). One day after adoptive transfer of progenitors, 1 × 10^6 human osteosarcoma cells were injected s.c. into the rear flank of mice in all four recipient groups. The tumor size was measured 10 days after injection. As shown in Figure 7B (right), mice receiving either CD34$^+$ hNeP or CD34$^-$ hNeP cells showed an increase in tumor growth compared with recipient mice receiving cMoP or PBS as a control. These data are concomitant with the mouse data shown in Figure 4B, suggesting that hNeP, the counterpart of mouse NeP, also are pro-tumoral and mediate solid tumor growth.

Finally, as we observed increased tumor size with hNeP adoptive transfer, we asked whether hNeP promoted tumor growth by blunting T cell activation. CD34$^+$ hNeP, CD34$^-$ hNeP, or mature neutrophils were FACS-sorted from fresh human BM and co-cultured with purified CD3$^+$ T cells isolated from other donor's blood in the presence of anti-CD3. At 24 hr after co-culture, mature neutrophils efficiently induced CD3$^+$ T cell activation as measured by CD69$^+$ expression (Figure 7C). CD3$^+$ T cells co-cultured with CD34$^+$ hNeP expressed very low levels of CD69 compared with the mature neutrophil co-culture group, suggesting significant induction of suppression in this group. CD34$^-$ hNeP inhibited T cell activation to a lesser extent compared with CD34$^+$ hNeP (Figure 7C). These data suggest that compared with mature neutrophils, hNeP are possibly immunosuppressive and promote tumorigenesis by attenuating tumor-destructive, pro-inflammatory T cell activation.

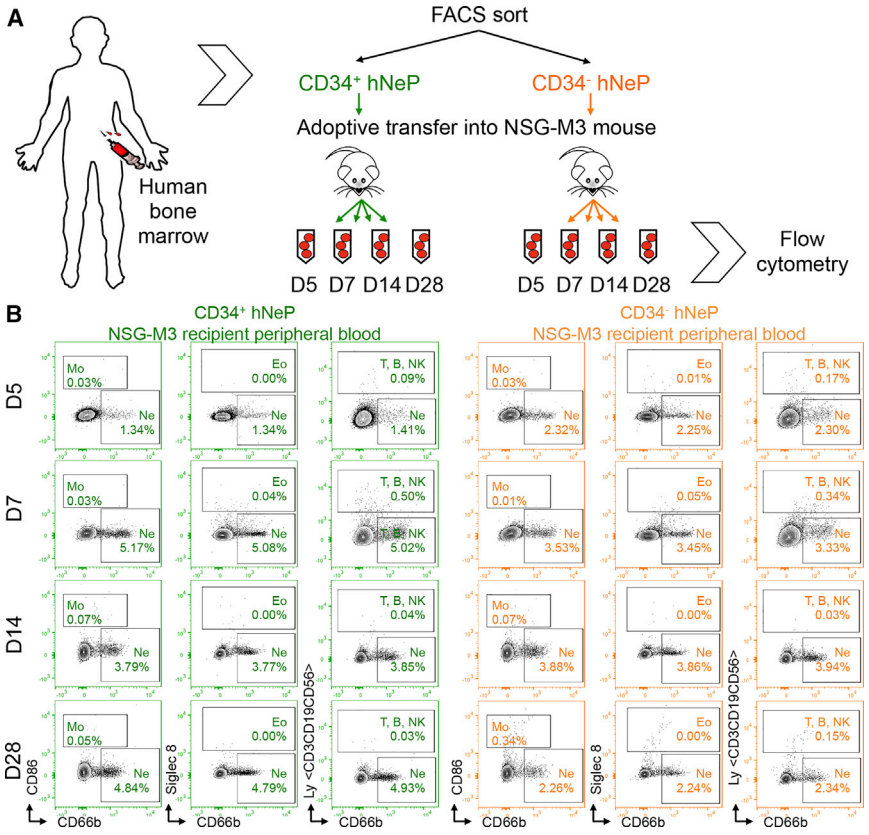

Figure 6. hNeP Produce Only Neutrophils in NSG-SGM3 Mice *In Vivo*

(A) Scheme showing the experimental procedure. $CD34^+$ hNeP and $CD34^-$ hNeP subsets identified in Figure 5C were sorted from healthy human BM and adoptively transferred into NSG-M3 recipient mice. Each recipient mouse received 25,000 donor human hNeP progenitor cells. After the transfer, peripheral blood was collected from each recipient via saphenous vein for flow cytometry on days (D) 5, 7, 14, and 28.

(B) Representative plots show the appearance of monocytes ($CD86^+$ $CD66b^-$), neutrophils ($CD86^-$ Siglec 8^- $CD66b^+$), eosinophils (Siglec 8^+), and lymphocytes (hLy^+) in each recipient group at the time points indicated. hLy antibody cocktail contains CD3, CD19, and CD56. N = 10 mice for each group. (See flow cytometry gating strategy in Figure S6C.)

DISCUSSION

In this paper, we report the discovery of a very early stage committed unipotent NeP that is present in mouse and human BM. We found that both the mouse and human NeP promoted primary tumor growth *in vivo* in established cancer models. Furthermore, we identified the presence of the human NeP (hNeP) in the blood of patients with recently diagnosed melanoma, suggesting that this hNeP is released from the BM in patients with cancer and can be readily identified in human blood.

Importantly, we found a tumor-promoting role for this early-stage NeP in both mice and humans. In tumor-bearing mice, frequencies of this NeP are increased in BM, suggesting aberrant myelopoiesis in response to tumor growth (Figure 4A). These results are consistent with previous studies that suggest that the tumor reprograms GMP to cause increased production of tumor-associated neutrophils (Casbon et al., 2015). Interestingly, we found that tumor-induced myelopoiesis is specific for NeP in mouse BM (Figure 4A). Furthermore, when adoptively transferred into recipient mice, the NeP significantly promoted melanoma tumor growth compared with other myeloid progenitors and was also found in the periphery as well as in the tumor, suggesting egress from the BM and infiltration to the tumor. Some of the #C1 and #C2 cells remain undifferentiated once they infiltrate into tumor and meanwhile start to express PD-L1 (Figures S5 and 4C). We also detected similar tumor-promoting effects of hNeP in human tumorigenesis using an NSG-humanized mouse model. After adoptive transfer, hNeP significantly promoted osteosarcoma tumor growth in NSG mice compared with other myeloid progenitors (Figure 7B). Importantly, we observed a 3- to 9-fold increase of hNeP in the blood of patients diagnosed with melanoma. This result is consistent with our observation of increased NeP in mouse periphery in response to tumor growth (Figure S5) and suggests that this hNeP could be used in some manner as a biomarker for early cancer detection.

The earliest committed NeP has remained elusive for decades. Most studies have focused on murine hematopoiesis. In this regard, the classic model of hematopoiesis shows that LSK^+ ($Lin^-CD117^+Ly6A/E^+CD127^-$) HSPCs give rise to CLP ($Lin^-CD117^{lo}Ly6A/E^+CD127^+$) for lymphopoiesis and to the $Lin^-CD117^+Ly6A/E^-CD127^-$ HSPCs for myelopoiesis (Weissman et al., 2001). A higher level of heterogeneity exists within the $lin^-CD117^+Ly6A/E^-CD127^-$ population, and the committed long-term monocyte progenitor partially overlaps with this HSPC fraction (Auffray et al., 2009; Olsson et al., 2016; Paul et al., 2015; Pronk et al., 2007). Indeed, further examination of the Lin^-CD117^+Ly6A/E^- HSPC fraction by mass cytometry showed five possibly committed myeloid progenitors (Figure 1A). Cluster #C in Figure 1A showed low to moderate expression of Ly6G, suggesting a neutrophil lineage potential for cells found within this cluster. This cluster was not identified in earlier hematopoiesis studies, as the neutrophil marker Ly6G was routinely excluded from flow cytometry panels at that time. ScRNA-seq analysis of this Ly6G-containing cluster #C further revealed two populations: an early-stage progenitor (#C1) with stem cell morphology and little Ly6G expression and a late-stage precursor (#C2) that expressed low levels of Ly6G with morphological features similar to transient neutrophil precursors (Figures 2D and S3B) (Evrard et al.,

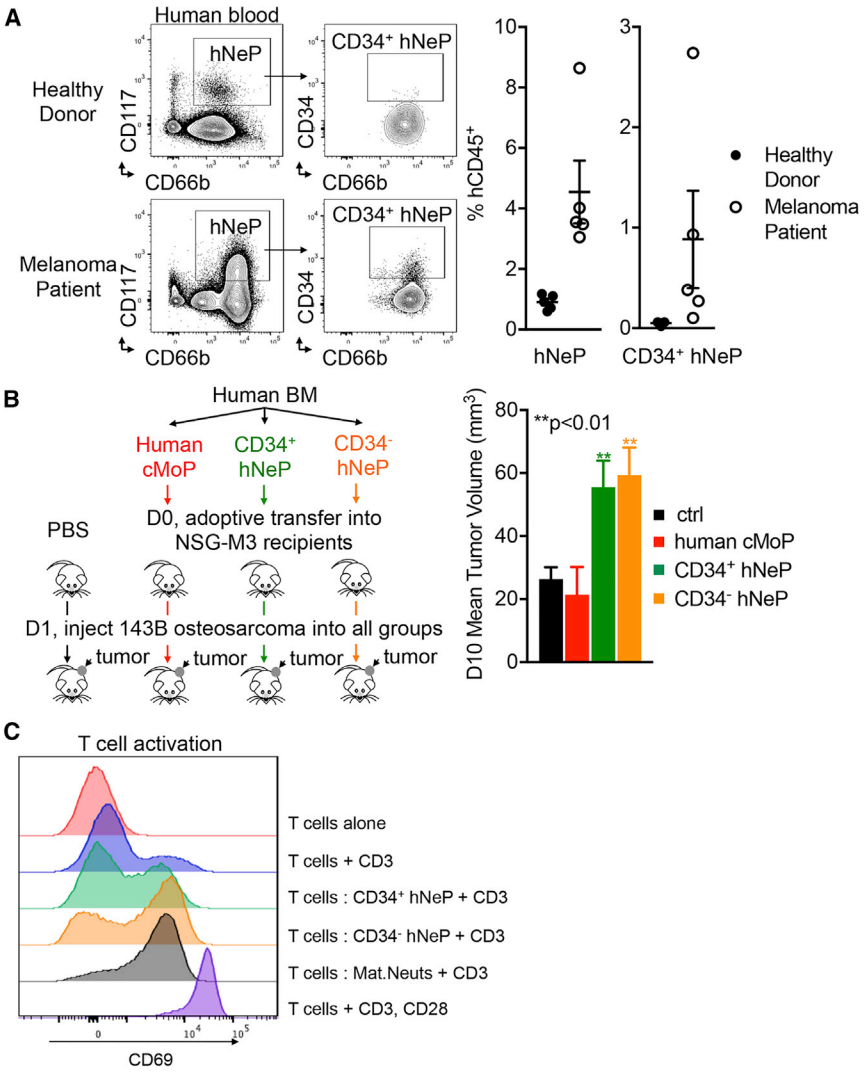

Figure 7. hNeP Is Increased in Melanoma Patient Blood and Promotes Early Osteosarcoma Tumor Growth in NSG-M3 Mice

(A) hNeP is increased in melanoma patient blood. hNeP frequency was detected by flow cytometry in peripheral blood collected from healthy donors (n = 5) and melanoma patients (n = 5). Error bars indicate mean ± SEM. (See donor information in Table S2.)

(B) Left: scheme showing the experiment procedure. $CD34^+$ hNeP subset, $CD34^-$ hNeP subset, and human cMoP were FACS-sorted from healthy human BM. The three populations were adoptively transferred into NSG-M3 recipient mice. Each recipient mouse received 25,000 donor human progenitor cells. Blank control group received only PBS for adoptive transfer. The next day, 1×10^6 143B human osteosarcoma cells were s.c. injected into each recipient mouse. Right: the tumor volume in each recipient was measured at 10 days post-injection. N = 5 mice in each group. Error bars indicate mean ± SEM.

(C) $CD34^+$ hNeP cells blunt T cell activation. FACS strategies for $CD34^+$ hNeP and $CD34^-$ hNeP are shown in Figures 5A and 5C using flow cytometry; FACS strategies for mature neutrophils is shown in Figure S7D using flow cytometry. Histogram overlay of CD69 for $CD3^+$ T cells cultured with $CD34^+$ hNeP, $CD34^-$ hNeP, and mature neutrophils, in the presence of anti-CD3 for 24 hr. $CD3^+$ T cells alone cultured without anti-CD3 served as the negative control group, and $CD3^+$ T cells alone cultured with anti-CD3, CD28 served as the positive control group for T cell activation.

2018; Satake et al., 2012; Sturge et al., 2015; Yáñez et al., 2015). Recently, a late-stage neutrophil precursor was identified in BM of mice (Kim et al., 2017). We located this population (termed by us as K.NeuP) on a viSNE map of Lin^-CD117^+Ly6A/E^- HSPCs (Figure S7A). Surprisingly, we found that this K.NeuP population was highly heterogeneous and contained other myeloid progenitors. From our mass cytometry data, we were able to generate a stringent flow cytometry gating strategy (Figure S7A) that allowed us to completely purify, with no contamination from other myeloid lineages, both #C1 (NeP) and #C2 cells (late-stage precursors) (Figure S7B) in order to demonstrate their neutrophil unipotency. We also located the recently reported mouse neutrophil precursor (termed by us as Ng.preNeu) (Evrard et al., 2018) and aligned it with #C1 (NeP) and #C2 in the neutrophil developmental branch. ViSNE analysis suggested the mouse Ng.preNeu shares phenotype that shares approximately 22% similarity to #C1 NeP and is mostly similar to #C2 (Figure S7C). The signature nuclear shape of the murine Ng.preNeu also closely resembles that of #C2 (Evrard et al., 2018). In addition, we compared the human Ng.preNeu (Evrard et al., 2018) with the hNeP that we have identified. The human Ng.preNeu does not express CD117 and CD34 and therefore does not overlap with the hNeP we identified (Figure S7D). Likely, the human Ng.preNeu represents a transient precursor between hNeP and terminally differentiated neutrophils. This hypothesis is supported by our analysis shown in Figure S7E that hNeP represents the lowest frequency (1%–3%) of human BM $CD45^+$ cells followed by Ng.preNeu (4%–10%), immature neutrophils 20%–40%, and mature neutrophils 30%–40%.

The lifespan of human neutrophils is better studied than is neutrophil heterogeneity. It is commonly recognized that the lifespan of neutrophils that are isolated by gradient separation varies from hours to days (Bekkering, 2013; Pillay et al., 2010). One possible hint we can take from this notion is that gradient isolation may yield a heterogeneous neutrophil population that contains neutrophil subsets and/or immature and mature neutrophils that are at different differentiation stages. Indeed, neutrophil heterogeneity has been suggested in both humans and mice (Beyrau et al., 2012; Silvestre-Roig et al., 2016). A few biological markers, such as CD49 or TCRα, β variants,

were suggested to identify certain neutrophil subsets in addition to neutrophil markers Ly6G (mouse) and CD66b (human) (Silvestre-Roig et al., 2016). However, neutrophil heterogeneity is still not well defined. In this study, we focused on the unipotency and the functions of NePs rather than the heterogeneity of the produced neutrophil progeny. Although we know that the identified NePs give rise to solely neutrophils, we have not yet studied whether these progenitors give rise to specific subsets of neutrophils, particularly in the setting of cancer. Hints from our data suggest that these hNeP NePs may promote tumor growth by suppressing T cell activation. Future studies will further examine the mechanisms by which these hNeP subsets influence T cell responses within the tumor microenvironment. We also do not exclude the possibility that the NeP itself, once egressed from the BM and present in the periphery, could directly participate in the tumor-promoting effects we observed (Figures 4 and 7).

In sum, using mass cytometry, we have identified an early-stage committed unipotent NeP that is present in both mouse and human BM. This discovery may drive new therapeutic and pharmaceutical targets for neutrophil-related diseases or treatment outcomes that are associated with chronic inflammation. For example, neutropenia leads to high susceptibility to infections and is often associated as a by-product of cancer treatments (Lyman et al., 2014). Targeting hNeP could rescue patients from undesirable neutropenia. In addition, our observation of increased hNeP in blood of melanoma patients could assist in early detection for cancer diagnosis as a biomarker. As this hNeP also displays tumor-promoting effects, we suggest the possibility that this hNeP itself could be an immune-oncology target, which opens a new field of therapeutic discovery.

STAR★METHODS

Detailed methods are provided in the online version of this paper and include the following:

- KEY RESOURCES TABLE
- CONTACT FOR REAGENT AND RESOURCE SHARING
- EXPERIMENTAL MODEL AND SUBJECT DETAILS
  - Mice
  - Human BM cells
  - Melanoma Patient Blood Collection
  - Human Peripheral Blood Collection
- METHOD DETAILS
  - Cell suspension for mass cytometry and flow cytometry
  - Mass Cytometry Antibodies
  - Mass Cytometry (CyTOF)
  - Flow Cytometry and Cell Sorting
  - Confocal Microscopy
  - Adoptive transfer
  - *In vitro* progenitor differentiation assay
  - Human T cell co-culture with NePs
  - Single-cell RNA-seq. 3′ end
  - Single cell RNA-Seq analysis
  - RNA-Seq
- QUANTIFICATION AND STATISTICAL ANALYSIS

SUPPLEMENTAL INFORMATION

Supplemental Information includes seven figures and two tables and can be found with this article online at https://doi.org/10.1016/j.celrep.2018.07.097.

ACKNOWLEDGMENTS

We would like to thank K. Ley, G.D. Thomas, R. Hanna, Z.C. Fan, and J. Xie for helpful discussions; D. Yoakum for assistance with mouse colony management; the La Jolla Institute (LJI) Histology Core for assistance with cell morphology experiments; J. Day and the LJI Sequencing Core for assistance with RNA sequencing; and the LJI Flow Cytometry Core for assistance with FACS. The Mass Cytometry Core was supported by NIH grant 1S10OD018499-01 (to C.K. and S.C.). The melanoma patient study was supported by National Cancer Institute Cancer Center Support Grant P30 CA168524 and used the Biospecimen Shared Resource. This work was supported by NIH grants R01HL134236, P01HL136275, and R01CA202987 (all to C.C.H) and ADA7-12-MN-31 (04) (to C.C.H. and Y.P.Z).

AUTHOR CONTRIBUTIONS

C.C.H. and Y.P.Z. conceptualized this project and wrote the manuscript. Y.P.Z. designed and performed the experiments, analyzed data, and prepared all figures. L.P. performed the T cell co-culture assay and analyzed data. H.Q.D. performed RNA-seq data analysis and PhenoGraph analysis of mass cytometry data. P.M. and R.W. helped with adoptive transfer and tumor experiments. A.B. helped with processing samples. E.E. and C.K. helped with mass cytometry experiments. Z.M. performed the confocal microscopy experiments. G.S., A.M., and P.V. performed the scRNA-seq experiments and data analysis. All authors reviewed and edited the manuscript.

DECLARATION OF INTERESTS

The authors declare no competing interests.

Received: March 3, 2018
Revised: June 18, 2018
Accepted: July 27, 2018
Published: August 28, 2018

REFERENCES

Akashi, K., Traver, D., Miyamoto, T., and Weissman, I.L. (2000). A clonogenic common myeloid progenitor that gives rise to all myeloid lineages. Nature *404*, 193–197.

Anderson, P.M. (2017). Immune therapy for sarcomas. Adv. Exp. Med. Biol. *995*, 127–140.

Arinobu, Y., Iwasaki, H., Gurish, M.F., Mizuno, S., Shigematsu, H., Ozawa, H., Tenen, D.G., Austen, K.F., and Akashi, K. (2005). Developmental checkpoints of the basophil/mast cell lineages in adult murine hematopoiesis. Proc. Natl. Acad. Sci. U S A *102*, 18105–18110.

Auffray, C., Fogg, D.K., Narni-Mancinelli, E., Senechal, B., Trouillet, C., Saederup, N., Leemput, J., Bigot, K., Campisi, L., Abitbol, M., et al. (2009). CX3CR1+ CD115+ CD135+ common macrophage/DC precursors and the role of CX3CR1 in their response to inflammation. J. Exp. Med. *206*, 595–606.

Avellino, R., Havermans, M., Erpelinck, C., Sanders, M.A., Hoogenboezem, R., van de Werken, H.J.G., Rombouts, E., van Lom, K., van Strien, P.M.H., Gebhard, C., et al. (2016). An autonomous CEBPA enhancer specific for myeloid-lineage priming and neutrophilic differentiation. Blood *127*, 2991–3003.

Bainton, D.F., Ullyot, J.L., and Farquhar, M.G. (1971). The development of neutrophilic polymorphonuclear leukocytes in human bone marrow. J. Exp. Med. *134*, 907–934.

Becher, B., Schlitzer, A., Chen, J., Mair, F., Sumatoh, H.R., Teng, K.W.W., Low, D., Ruedl, C., Riccardi-Castagnoli, P., Poidinger, M., et al. (2014).

High-dimensional analysis of the murine myeloid cell system. Nat. Immunol. *15*, 1181–1189.

Bekkering, S. (2013). Another look at the life of a neutrophil. World J. Hepatol. *2*, 44.

Bendall, S.C., Simonds, E.F., Qiu, P., Amir, A.D., Krutzik, P.O., Finck, R., Bruggner, R.V., Melamed, R., Trejo, A., Ornatsky, O.I., et al. (2011). Single-cell mass cytometry of differential immune and drug responses across a human hematopoietic continuum. Science *332*, 687–696.

Beyrau, M., Bodkin, J.V., and Nourshargh, S. (2012). Neutrophil heterogeneity in health and disease: a revitalized avenue in inflammation and immunity. Open Biol. *2*, 120134.

Billerbeck, E., Barry, W.T., Mu, K., Dorner, M., Rice, C.M., and Ploss, A. (2011). Development of human CD4+FoxP3+ regulatory T cells in human stem cell factor-, granulocyte-macrophage colony-stimulating factor-, and interleukin-3-expressing NOD-SCID IL2Rγ(null) humanized mice. Blood *117*, 3076–3086.

Borregaard, N. (2010). Neutrophils, from marrow to microbes. Immunity *33*, 657–670.

Buenrostro, J.D., Corces, M.R., Lareau, C.A., Wu, B., Schep, A.N., Aryee, M.J., Majeti, R., Chang, H.Y., and Greenleaf, W.J. (2018). Integrated single-cell analysis maps the continuous regulatory landscape of human hematopoietic differentiation. Cell *173*, 1535–1548.e16.

Casbon, A.-J., Reynaud, D., Park, C., Khuc, E., Gan, D.D., Schepers, K., Passegué, E., and Werb, Z. (2015). Invasive breast cancer reprograms early myeloid differentiation in the bone marrow to generate immunosuppressive neutrophils. Proc. Natl. Acad. Sci. U S A *112*, E566–E575.

Chen, H., Lau, M.C., Wong, M.T., Newell, E.W., Poidinger, M., and Chen, J. (2016). Cytofkit: a Bioconductor package for an integrated mass cytometry data analysis pipeline. PLoS Comput. Biol. *12*, e1005112.

Coughlan, A.M., Harmon, C., Whelan, S., O'Brien, E.C., O'Reilly, V.P., Crotty, P., Kelly, P., Ryan, M., Hickey, F.B., O'Farrelly, C., and Little, M.A. (2016). Myeloid engraftment in humanized mice: impact of granulocyte-colony stimulating factor treatment and transgenic mouse strain. Stem Cells Dev. *25*, 530–541.

Doulatov, S., Notta, F., Eppert, K., Nguyen, L.T., Ohashi, P.S., and Dick, J.E. (2010). Revised map of the human progenitor hierarchy shows the origin of macrophages and dendritic cells in early lymphoid development. Nat. Immunol. *11*, 585–593.

Doulatov, S., Notta, F., Laurenti, E., and Dick, J.E. (2012). Hematopoiesis: a human perspective. Cell Stem Cell *10*, 120–136.

Edvardsson, L., Dykes, J., and Olofsson, T. (2006). Isolation and characterization of human myeloid progenitor populations—TpoR as discriminator between common myeloid and megakaryocyte/erythroid progenitors. Exp. Hematol. *34*, 599–609.

Elghetany, M.T., Ge, Y., Patel, J., Martinez, J., and Uhrova, H. (2004). Flow cytometric study of neutrophilic granulopoiesis in normal bone marrow using an expanded panel of antibodies: correlation with morphologic assessments. J. Clin. Lab. Anal. *18*, 36–41.

Evrard, M., Kwok, I.W.H., Chong, S.Z., Teng, K.W.W., Becht, E., Chen, J., Sieow, J.L., Penny, H.L., Ching, G.C., Devi, S., et al. (2018). Developmental analysis of bone marrow neutrophils reveals populations specialized in expansion, trafficking, and effector functions. Immunity *48*, 364–379.e8.

Fiedler, K., and Brunner, C. (2012). The role of transcription factors in the guidance of granulopoiesis. Am. J. Blood Res. *2*, 57–65.

Finck, R., Simonds, E.F., Jager, A., Krishnaswamy, S., Sachs, K., Fantl, W., Pe'er, D., Nolan, G.P., and Bendall, S.C. (2013). Normalization of mass cytometry data with bead standards. Cytometry A *83*, 483–494.

Fogg, D.K., Sibon, C., Miled, C., Jung, S., Aucouturier, P., Littman, D.R., Cumano, A., and Geissmann, F. (2006). A clonogenic bone marrow progenitor specific for macrophages and dendritic cells. Science *311*, 83–87.

Hagerling, C., and Werb, Z. (2016). Neutrophils: critical components in experimental animal models of cancer. Semin. Immunol. *28*, 197–204.

Hettinger, J., Richards, D.M., Hansson, J., Barra, M.M., Joschko, A.-C., Krijgsveld, J., and Feuerer, M. (2013). Origin of monocytes and macrophages in a committed progenitor. Nat. Immunol. *14*, 821–830.

Hoebeke, I., De Smedt, M., Stolz, F., Pike-Overzet, K., Staal, F.J.T., Plum, J., and Leclercq, G. (2007). T-, B- and NK-lymphoid, but not myeloid cells arise from human CD34(+)CD38(-)CD7(+) common lymphoid progenitors expressing lymphoid-specific genes. Leukemia *21*, 311–319.

Horman, S.R., Velu, C.S., Chaubey, A., Bourdeau, T., Zhu, J., Paul, W.E., Gebelein, B., and Grimes, H.L. (2009). Gfi1 integrates progenitor versus granulocytic transcriptional programming. Blood *113*, 5466–5475.

Huang, J., Xiao, Y., Xu, A., and Zhou, Z. (2016). Neutrophils in type 1 diabetes. J. Diabetes Investig. *7*, 652–663.

Kawamura, S., Onai, N., Miya, F., Sato, T., Tsunoda, T., Kurabayashi, K., Yotsumoto, S., Kuroda, S., Takenaka, K., Akashi, K., and Ohteki, T. (2017). Identification of a human clonogenic progenitor with strict monocyte differentiation potential: a counterpart of mouse cMoPs. Immunity *46*, 835–848.e4.

Kim, M.-H., Yang, D., Kim, M., Kim, S.-Y., Kim, D., and Kang, S.-J. (2017). A late-lineage murine neutrophil precursor population exhibits dynamic changes during demand-adapted granulopoiesis. Sci. Rep. *7*, 39804.

Kohn, L.A., Hao, Q.-L., Sasidharan, R., Parekh, C., Ge, S., Zhu, Y., Mikkola, H.K.A., and Crooks, G.M. (2012). Lymphoid priming in human bone marrow begins before expression of CD10 with upregulation of L-selectin. Nat. Immunol. *13*, 963–971.

Lee, P.Y., Wang, J.-X., Parisini, E., Dascher, C.C., and Nigrovic, P.A. (2013). Ly6 family proteins in neutrophil biology. J. Leukoc. Biol. *94*, 585–594.

Lee, J., Breton, G., Oliveira, T.Y.K., Zhou, Y.J., Aljoufi, A., Puhr, S., Cameron, M.J., Sékaly, R.-P., Nussenzweig, M.C., and Liu, K. (2015). Restricted dendritic cell and monocyte progenitors in human cord blood and bone marrow. J. Exp. Med. *212*, 385–399.

Levine, J.H., Simonds, E.F., Bendall, S.C., Davis, K.L., Amir, A.D., Tadmor, M.D., Litvin, O., Fienberg, H.G., Jager, A., Zunder, E.R., et al. (2015). Data-driven phenotypic dissection of AML reveals progenitor-like cells that correlate with prognosis. Cell *162*, 184–197.

Liao, Y., Smyth, G.K., and Shi, W. (2013). The Subread aligner: fast, accurate and scalable read mapping by seed-and-vote. Nucleic Acids Res. *41*, e108.

Liao, Y., Smyth, G.K., and Shi, W. (2014). featureCounts: an efficient general purpose program for assigning sequence reads to genomic features. Bioinformatics *30*, 923–930.

Liu, K., Victora, G.D., Schwickert, T.A., Guermonprez, P., Meredith, M.M., Yao, K., Chu, F.-F., Randolph, G.J., Rudensky, A.Y., and Nussenzweig, M. (2009). In vivo analysis of dendritic cell development and homeostasis. Science *324*, 392–397.

Lyman, G.H., Abella, E., and Pettengell, R. (2014). Risk factors for febrile neutropenia among patients with cancer receiving chemotherapy: A systematic review. Crit. Rev. Oncol. Hematol. *90*, 190–199.

Manz, M.G., Miyamoto, T., Akashi, K., and Weissman, I.L. (2002). Prospective isolation of human clonogenic common myeloid progenitors. Proc. Natl. Acad. Sci. U S A *99*, 11872–11877.

Mori, Y., Iwasaki, H., Kohno, K., Yoshimoto, G., Kikushige, Y., Okeda, A., Uike, N., Niiro, H., Takenaka, K., Nagafuji, K., et al. (2009). Identification of the human eosinophil lineage-committed progenitor: revision of phenotypic definition of the human common myeloid progenitor. J. Exp. Med. *206*, 183–193.

Notta, F., Zandi, S., Takayama, N., Dobson, S., Gan, O.I., Wilson, G., Kaufmann, K.B., McLeod, J., Laurenti, E., Dunant, C.F., et al. (2016). Distinct routes of lineage development reshape the human blood hierarchy across ontogeny. Science *351*, aab2116.

Olsson, A., Venkatasubramanian, M., Chaudhri, V.K., Aronow, B.J., Salomonis, N., Singh, H., and Grimes, H.L. (2016). Single-cell analysis of mixed-lineage states leading to a binary cell fate choice. Nature *537*, 698–702.

Paul, F., Arkin, Y., Giladi, A., Jaitin, D.A., Kenigsberg, E., Keren-Shaul, H., Winter, D., Lara-Astiaso, D., Gury, M., Weiner, A., et al. (2015). Transcriptional heterogeneity and lineage commitment in myeloid progenitors. Cell *163*, 1663–1677.

Pillay, J., den Braber, I., Vrisekoop, N., Kwast, L.M., de Boer, R.J., Borghans, J.A.M., Tesselaar, K., and Koenderman, L. (2010). In vivo labeling with $2H_2O$ reveals a human neutrophil lifespan of 5.4 days. Blood *116*, 625–627.

Pronk, C.J.H., Rossi, D.J., Månsson, R., Attema, J.L., Norddahl, G.L., Chan, C.K.F., Sigvardsson, M., Weissman, I.L., and Bryder, D. (2007). Elucidation of the phenotypic, functional, and molecular topography of a myeloerythroid progenitor cell hierarchy. Cell Stem Cell *1*, 428–442.

Qi, X., Hong, J., Chaves, L., Zhuang, Y., Chen, Y., Wang, D., Chabon, J., Graham, B., Ohmori, K., Li, Y., and Huang, H. (2013). Antagonistic regulation by the transcription factors C/EBPα and MITF specifies basophil and mast cell fates. Immunity *39*, 97–110.

Radomska, H.S., Huettner, C.S., Zhang, P., Cheng, T., Scadden, D.T., and Tenen, D.G. (1998). CCAAT/enhancer binding protein alpha is a regulatory switch sufficient for induction of granulocytic development from bipotential myeloid progenitors. Mol. Cell. Biol. *18*, 4301–4314.

Rizzo, M.L. (2016). Statistical Computing with R (Boca Raton, FL: CRC Press).

Robinson, M.D., McCarthy, D.J., and Smyth, G.K. (2010). edgeR: a Bioconductor package for differential expression analysis of digital gene expression data. Bioinformatics *26*, 139–140.

Sagiv, J.Y., Michaeli, J., Assi, S., Mishalian, I., Kisos, H., Levy, L., Damti, P., Lumbroso, D., Polyansky, L., Sionov, R.V., et al. (2015). Phenotypic diversity and plasticity in circulating neutrophil subpopulations in cancer. Cell Rep. *10*, 562–573.

Samusik, N., Good, Z., Spitzer, M.H., Davis, K.L., and Nolan, G.P. (2016). Automated mapping of phenotype space with single-cell data. Nat. Methods *13*, 493–496.

Satake, S., Hirai, H., Hayashi, Y., Shime, N., Tamura, A., Yao, H., Yoshioka, S., Miura, Y., Inaba, T., Fujita, N., et al. (2012). C/EBPβ is involved in the amplification of early granulocyte precursors during candidemia-induced "emergency" granulopoiesis. J. Immunol. *189*, 4546–4555.

Satija, R., Farrell, J.A., Gennert, D., Schier, A.F., and Regev, A. (2015). Spatial reconstruction of single-cell gene expression data. Nat. Biotechnol. *33*, 495–502.

Satoh, T., Nakagawa, K., Sugihara, F., Kuwahara, R., Ashihara, M., Yamane, F., Minowa, Y., Fukushima, K., Ebina, I., Yoshioka, Y., et al. (2017). Identification of an atypical monocyte and committed progenitor involved in fibrosis. Nature *541*, 96–101.

Silvestre-Roig, C., Hidalgo, A., and Soehnlein, O. (2016). Neutrophil heterogeneity: implications for homeostasis and pathogenesis. Blood *127*, 2173–2181.

Soehnlein, O., Steffens, S., Hidalgo, A., and Weber, C. (2017). Neutrophils as protagonists and targets in chronic inflammation. Nat. Rev. Immunol. *17*, 248–261.

Sturge, C.R., Burger, E., Raetz, M., Hooper, L.V., and Yarovinsky, F. (2015). Cutting edge: developmental regulation of IFN-γ production by mouse neutrophil precursor cells. J. Immunol. *195*, 36–40.

Summers, C., Rankin, S.M., Condliffe, A.M., Singh, N., Peters, A.M., and Chilvers, E.R. (2010). Neutrophil kinetics in health and disease. Trends Immunol. *31*, 318–324.

Terstappen, L.W., and Loken, M.R. (1990). Myeloid cell differentiation in normal bone marrow and acute myeloid leukemia assessed by multi-dimensional flow cytometry. Anal. Cell. Pathol. *2*, 229–240.

van der Maaten, L., and Hinton, G. (2008). Visualizing data using t-SNE. J. Mach. Learn. Res. *9*, 85.

Weiskopf, K., Schnorr, P.J., Pang, W.W., Chao, M.P., Chhabra, A., Seita, J., Feng, M., and Weissman, I.L. (2016). Myeloid cell origins, differentiation, and clinical implications. Microbiol. Spectr. *4*, 4.

Weissman, I.L., Anderson, D.J., and Gage, F. (2001). Stem and progenitor cells: origins, phenotypes, lineage commitments, and transdifferentiations. Annu. Rev. Cell Dev. Biol. *17*, 387–403.

Yáñez, A., Ng, M.Y., Hassanzadeh-Kiabi, N., and Goodridge, H.S. (2015). IRF8 acts in lineage-committed rather than oligopotent progenitors to control neutrophil vs monocyte production. Blood *125*, 1452–1459.

Zhang, D.E., Zhang, P., Wang, N.D., Hetherington, C.J., Darlington, G.J., and Tenen, D.G. (1997). Absence of granulocyte colony-stimulating factor signaling and neutrophil development in CCAAT enhancer binding protein alpha-deficient mice. Proc. Natl. Acad. Sci. U S A *94*, 569–574.

Zhang, J.Q., Biedermann, B., Nitschke, L., and Crocker, P.R. (2004). The murine inhibitory receptor mSiglec-E is expressed broadly on cells of the innate immune system whereas mSiglec-F is restricted to eosinophils. Eur. J. Immunol. *34*, 1175–1184.

Zheng, G.X.Y., Terry, J.M., Belgrader, P., Ryvkin, P., Bent, Z.W., Wilson, R., Ziraldo, S.B., Wheeler, T.D., McDermott, G.P., Zhu, J., et al. (2017). Massively parallel digital transcriptional profiling of single cells. Nat. Commun. *8*, 14049.

STAR★METHODS

KEY RESOURCES TABLE

REAGENT or RESOURCE	SOURCE	IDENTIFIER
CyTOF Antibodies (mouse)		
Anti-Mouse CD45 (Clone 30-F11) −89Y	Fluidigm	Cat# 3089005B
Anti-mouse TER-119/Erythroid Cells (Clone TER-119)-MaxPar® Ready	Biolegend	Cat# 116241; RRID:AB_2563789
Anti-mouse CD41 (Clone MWReg30)-MaxPar® Ready	Biolegend	Cat# 133919; RRID:AB_2565433
Anti-mouse CD127 (IL-7Rα) (Clone A7R34)-MaxPar® Ready	Biolegend	Cat# 135029; RRID:AB_2563716
Anti-mouse CD335 (NKp46) (Clone 29A1.4)-MaxPar® Ready	Biolegend	Cat# 137625; RRID:AB_2563744
Anti-Mouse CD11c (Clone N418)-142Nd	Fluidigm	Cat# 3142003B
Anti-Mouse TCRβ (Clone H57-597)-143Nd	Fluidigm	Cat# 3143010B
Anti-mouse GM-CSF (MP1-22E9 (RUO))-Purified	BD Biosciences	Cat# 554404; RRID:AB_395370
Anti-mouse Ly-6G (Clone 1A8)-MaxPar® Ready	Biolegend	Cat# 127637; RRID:AB_2563784
Anti-Mouse CD43 (Clone S11)-146Nd	Fluidigm	Cat# 3146009B
Anti-mouse CD105 (Clone MJ7/18)-Purified	Biolegend	Cat# 120402; RRID:AB_961070
Anti-Mouse CD11b (Clone M1/70)-148Nd	Fluidigm	Cat# 3148003B
Anti-mouse CD62L (Clone MEL-14)-MaxPar® Ready	Biolegend	Cat# 104443; RRID:AB_2562802
Anti-mouse Ly-6C (Clone HK1.4)-MaxPar® Ready	Biolegend	Cat# 128039; RRID:AB_2563783
Anti-mouse CD16/32 (Clone 93)-MaxPar® Ready	Biolegend	Cat# 101335; RRID:AB_2563723
Anti-mouseCD135 (Flt3) (Clone A2F10)-Purified	ThermoFisher	Cat# 14-1351-82; RRID:AB_467481
Anti-mouseCD71 (Clone RI7217)-Purified	Biolegend	Cat# 113802; RRID:AB_313563
Anti-mouse CD182 (CXCR2) (Clone SA044G4)-Purified	Biolegend	Cat# 149302; RRID:AB_2565277
Anti-Mouse Ly6B (Clone 7/4)-Purified	abcam	Cat# ab53457; RRID:AB_881409
Anti-Mouse CD48 (Clone HM48.1)-156Gd	Fluidigm	Cat# 3156012B
Anti-mouse CD34 (Clone MEC14.7)-Purified	Biolegend	Cat# 119302; RRID:AB_345280
Anti-Mouse F4/80 (Clone BM8)-159Tb	Fluidigm	Cat# 3159009B
Anti-mouse CD169 (Siglec-1) (Clone 3D6.112)-Purified	Biolegend	Cat# 142402; RRID:AB_10916523
Anti-mouse CD115 (CSF-1R) (Clone AFS98)-Purified	Biolegend	Cat# 135502; RRID:AB_1937293
Anti-Mouse Siglec-F (Clone E50-2440 (RUO))-Purified	BD Biosciences	Cat# 552125; RRID:AB_394340
Anti-mouse FcεRIα (Clone MAR-1)-MaxPar® Ready	Biolegend	Cat# 134321; RRID:AB_2563768
Anti-mouse CD183 (Clone CXCR3-173)-Purified	Biolegend	Cat# 126502; RRID:AB_1027635
Anti-Mouse NK1.1 (Clone PK136)-165Ho	Fluidigm	Cat# 3165018B
Anti-Mouse CD117/c-kit (Clone 2B8)-166Er	Fluidigm	Cat# 3166004B
Anti-Mouse CD150 (Clone TC1512F12.2)-167Er	Fluidigm	Cat# 3167004B
Anti-Mouse Ki67 (Clone B56 (RUO))-Purified	BD Biosciences	Cat# 556003; RRID:AB_396287
Anti-Mouse Ly-6A/E (Sca-1) (Clone D7)-169Tm	Fluidigm	Cat# 3169015B
Anti-Mouse CD162 (Clone 4RA10 (RUO))-Purified	BD Biosciences	Cat# 557787; RRID:AB_647340
Anti-mouse CD11a (Clone M17/4)-Purified	Biolegend	Cat# 101101; RRID:AB_312774
Anti-mouse CD90 (Clone G7)-Purified	Biolegend	Cat# 105202; RRID:AB_313169
Anti-Mouse I-A/I-E (Clone M5/114.15.2)-174Yb	Fluidigm	Cat# 3174003B
Anti-mouse CD16.2 (FcγRIV) (Clone 9E9)-Purified	Biolegend	Cat# 149502; RRID:AB_2565302
Anti-Human/Mouse CD45R/B220 (Clone RA36B2)-176Yb	Fluidigm	Cat# 3176002B
Flow Cytometry antibodies (mouse)		
Anti-mouse CD3ε (Clone 145-2C11)-APC-Cy7	BD Biosciences	Cat# 557596; RRID:AB_396759
Anti-mouse CD19 (Clone 1D3)-APC-Cy7	BD Biosciences	Cat# 557655; RRID:AB_396770

(*Continued on next page*)

Continued

REAGENT or RESOURCE	SOURCE	IDENTIFIER
Anti-mouse CD161 (Clone PK136)- APC-eFluor® 780	ThermoFisher	Cat# 47-5941-82; RRID:AB_10853969
Anti-mouse F4/80 (Clone T45-2342)-PE-CF594	BD Biosciences	Cat# 565613
Anti-mouse/human CD11b (Clone M1/70)-Brilliant Violet 605	BioLegend	Cat# 101257; RRID:AB_2565431
Anti-mouse CD11a (Clone M17/4)-APC	BioLegend	Cat#101120; RRID:AB_2562779
Anti-mouse CD11c (Clone HL3)-APC-Cy7	BD Biosciences	Cat# 561241; RRID:AB_10611727
Anti-mouse CD45 (Clone 30-F11)- Brilliant Violet 570	BioLegend	Cat# 103135; RRID:AB_10898325
Anti-mouse CD45 (Clone 30-F11)- Brilliant Violet 605	BioLegend	Cat# 103139; RRID:AB_2562341
Anti-mouse CD45.1 (Clone A20)-PerCP/Cy5.5	BioLegend	Cat# 110728; RRID:AB_893346
Anti-mouse CD45.2 (Clone 104)-FITC	BioLegend	Cat# 109806; RRID:AB_313443
Anti-mouse CD117 (c-kit) (Clone 2B8)-PE	BioLegend	Cat# 105808; RRID:AB_313217
Anti-mouse CD117 (c-kit) (Clone 2B8)-APC-R700	BD Biosciences	Cat# 565476
Anti-mouse Ly6A/E (Sca-1) (Clone D7)- Brilliant Violet 785	BioLegend	Cat# 108139; RRID:AB_2565957
Anti-mouse CD16/32 (FcγRIII/II) (Clone 2.4G2)-APC-R700	BD Biosciences	Cat# 565502
Anti-mouse CD16/32 (FcγRIII/II) (Clone 93)-FITC	BioLegend	Cat# 101306; RRID:AB_312805
Anti-mouse CD16/32 (FcγRIII/II) (Clone 2.4G2)-Purified NA/LE	BD Biosciences	Cat# 553140
Anti-mouse CD41 (Clone MWReg30)-APC-Cy7	BioLegend	Cat# 133928; RRID:AB_2572132
Anti-mouse CD115 (M-CSFR) (Clone AFS98;)- Brilliant Violet 421	BioLegend	Cat# 135513; RRID:AB_2562667
Anti-mouse CD127 (IL-7Rα) (Clone A7R34)-APC/Cy7	BioLegend	Cat# 135040; RRID:AB_2566161
Anti-mouse CD127 (IL-7Rα) (Clone A7R34)-PE/Dazzle 594	BioLegend	Cat# 135032; RRID:AB_2564217
Anti-Mouse CD162 (Clone 2PH1)-BV510	BD Biosciences	Cat# 563448
Anti-mouse Ter119 (Clone TER-119)-APC-Cy7	BioLegend	Cat# 116223; RRID:AB_2137788
Anti-mouse Ly6B (Clone 7/4)-FITC	Abcam	Cat# ab53453; RRID:AB_881408
Anti-mouse Ly6G (Clone 1A8)-FITC	BioLegend	Cat# 127606; RRID:AB_1236494
Anti-mouse Ly6G (Clone 1A8)-PE	BioLegend	Cat# 127608; RRID:AB_1186099
Anti-mouse CD48 (Clone HM48-1)-PE/Cy7	BioLegend	Cat# 103424; RRID:AB_2075049
Anti-mouse Ly6C (Clone HK1.4)-PerCP/Cy5.5	BioLegend	Cat# 128012; RRID:AB_1659241
Anti-mouse Siglec F (Clone E50-2446)-Alexa Fluor® 647	BD Biosciences	Cat# 562680; RRID:AB_2687570
Anti-mouse Siglec F (Clone E50-2446)-PE-CF594	BD Biosciences	Cat# 562757; RRID:AB_2687994
Anti-mouse FcεRIα (Clone MAR-1)-Alexa Fluor® 647	BioLegend	Cat# 134310; RRID:AB_1626093
Rabbit anti-Ki67 monoclonal antibody (Clone SP6)	Abcam	Cat# ab16667; RRID:AB_302459
Anti-rabbit IgG (H+L), F(ab')2 Fragment (Alexa Fluor®647 Conjugate)	CellSignaling	Cat#4414; RRID:AB_10693544
Flow Cytometry antibodies (human)		
Anti-human CD45 (Clone 2D1)-Brilliant Violet 570	BioLegend	Cat#304034; RRID:AB_2563426
Anti-human CD3ε (Clone HIT3a)- BB515	BD Biosciences	Cat# 565100
Anti-human CD3ε (Clone OKT3)- Alexa Fluor® 647	BD Biosciences	Cat# 566686
Anti-human CD3ε (Clone HIT3a)- PerCP/Cy5.5	BioLegend	Cat# 300328; RRID:AB_1575008
Anti-human CD7 (Clone M-T701)-BB515	BD Biosciences	Cat# 565211
Anti-human CD10 (Clone HI10a)-FITC	BioLegend	Cat#312208; RRID:AB_314919
Anti-human CD11c (Clone B-ly6)-BB515	BD Biosciences	Cat# 564490
Anti-human CD19 (Clone HIB19)-BB515	BD Biosciences	Cat# 564456
Anti-human CD19 (Clone SJ25C1)-PerCP/Cy5.5	BioLegend	Cat# 363016; RRID:AB_2564207
Anti-human CD161 (Clone HP-3G10)-FITC	BioLegend	Cat# 339936; RRID:AB_2564140
Anti-human CD56 (Clone B159)-BB515	BD Biosciences	Cat# 564488
Anti-human CD56 (NCAM) (Clone MEM-188)-PerCP/Cy5.5	BioLegend	Cat# 304626; RRID:AB_10641700
Anti-human CD90 (Thy1) (Clone 5E10)-FITC	BioLegend	Cat#328108; RRID:AB_893429

(*Continued on next page*)

Continued

REAGENT or RESOURCE	SOURCE	IDENTIFIER
Anti-human CD127 (IL-7Rα) (Clone A019D5)-FITC	BioLegend	Cat# 351312; RRID:AB_10897643
Anti-human CD235a (Clone GA-R2)-BB515	BD Biosciences	Cat# 565233
Anti-human CD41a (Clone HIP8)-BB515	BD Biosciences	Cat# 565237; RRID:AB_2721014
Anti-Human Siglec-1 (CD169)(Clone 7-239)-BB515	BD Biosciences	Cat#565353
Anti-human CD69 (Clone FN50)-APC	BioLegend	Cat#310910; RRID:AB_314845
Anti-human CD86 (Clone IT2.2)- Brilliant Violet 605	BioLegend	Cat# 305430; RRID:AB_2563824
Anti-human CD14 (Clone 63D3)-APC/Cy7	BioLegend	Cat# 367108; RRID:AB_2566710
Anti-human HLA-DR (Clone L243)-PE/Cy7	BioLegend	Cat# 307616; RRID:AB_493588
Anti-human CD16 (Clone 3G8)-Brilliant Violet 785	BioLegend	Cat#302046; RRID:AB_2563803
Anti-human CD66b (Clone G10F5)-PE	BioLegend	Cat# 305106; RRID:AB_2077857
Anti-human CD34 (Clone 581)-BV421	BD Biosciences	Cat#562577; RRID:AB_2687922
Anti-human CD117 (c-kit) (Clone YB5.B8)- APC-R700	BD Biosciences	Cat# 565195; RRID:AB_2716871
Anti-human CD117 (c-kit) (Clone 104D2)-Brilliant Violet 711	BioLegend	Cat# 313230; RRID:AB_2566217
Anti-human CD38 (Clone HB-7)- PE/Dazzle 594	BioLegend	Cat# 356630; RRID:AB_2650757
Anti-human CD15 (SSEA-1) (Clone W6D3)-Alexa Fluor® 700	BioLegend	Cat#323026; RRID:AB_2561427
Anti-human CD15 (SSEA-1) (Clone W6D3)-Brilliant Violet 605	BioLegend	Cat#323032; RRID:AB_2562132
Anti-human CD49d (Clone 9F10)-APC	BioLegend	Cat# 304308; RRID:AB_2130041
Anti-human CD49d (Clone 9F10)-Brilliant Violet 711	BioLegend	Cat# 304308; RRID:AB_2687198
Anti-human CD101 (Clone BB27)-PE/Cy7	BioLegend	Cat# 331014; RRID:AB_2716109
Anti-human Siglec 8 (Clone 7C9)-FITC	Miltenyi Biotec	Cat#130-098-715; RRID:AB_2653427
Anti-human Siglec 8 (Clone 7C9)-APC	BioLegend	Cat#347106; RRID:AB_2561402
Anti-human FcεRIα (Clone AER-37)-APC	BioLegend	Cat#334612; RRID:AB_10578086
Anti-human FcεRIα (Clone AER-37)-FITC	BioLegend	Cat# 334608; RRID:AB_1227653
Biological Samples		
Healthy human BM	AllCells, Inc.	Cat# ABM001
Healthy human peripheral blood	La Jolla Institute for Allergy and Immunology, Clinical studies core, Normal Blood Donor Program (NBDP)	https://www.lji.org/faculty-research/scientific-cores/clinical-studies
Melanoma patient peripheral blood	University of Kansas Cancer Center, Biospecimen Repository Core Facility (BRCF)	http://www.kumc.edu/school-of-medicine/biospecimen.html
Chemicals, Peptides, and Recombinant Proteins		
eBioscience 1X RBC Lysis Buffer	ThermoFisher	Cat# 00-4333-57
HyClone Phosphate Buffered Saline solution	GE Lifesciences	Cat#SH30256.01
Ethylenediaminetetraacetic acid (EDTA)	ThermoFisher	Cat# AM9260G
Trypsin EDTA 1X	Corning	Cat# 25-053-CI
Human AB Serum, Heat Inactivated	Omega Scientific	Cat# HS-25
Bovine Serum Albumin	Sigma-Aldrich	Cat# A4503
Fetal Bovine Serum	Omega Scientific	Cat# FB-02
Donkey Serum	Sigma-Aldrich	Cat# S30-M
Sodium azide	Sigma-Aldrich	Cat# S2002
Triton X-100	Sigma-Aldrich	Cat# X100
ProLong Gold Antifade Mountant	ThermoFisher	Cat# P10144
Antibody Stabilizer	CANDOR Bioscience	Cat# 130050
MAXPAR® Antibody Labeling Kits	Fluidigm	http://www.dvssciences.com/product-catalog-maxpar.php

(*Continued on next page*)

Continued

REAGENT or RESOURCE	SOURCE	IDENTIFIER
Cisplatin-194Pt	Fluidigm	Cat# 201194
Intercalator-Ir	Fluidigm	Cat# 201192B
eBioscience Foxp3 / Transcription Factor Staining Buffer Set	ThermoFisher	Cat# 00-5523-00
EQ Four Element Calibration Beads	Fluidigm	Cat# 201078
Hoechst	ThermoFisher	Cat# H1399
Dimethyl sulphoxide	Sigma-Aldrich	Cat# D5879
Paraformaldehyde	Sigma-Aldrich	Cat# 158127
MethoCult GF M3434	Stem Cell Technologies	Cat# 03434
DMEM–Dulbecco's Modified Eagle Medium	ThermoFisher	Cat#11995065
HEPES buffer	Corning	Cat# 25-06-CI
Critical Commercial Assays		
LIVE/DEAD Fixable Blue Dead Cell Stain Kit	ThermoFisher	Cat# L23105
LIVE/DEAD Fixable Yellow Dead Cell Stain Kit	ThermoFisher	Cat# L34968
TRIzol Plus RNA Purification Kit	ThermoFisher	Cat# 12183555
Chromium Single Cell 3′ v2 Reagent Kits	10x Genomics	Cat# PN-120237
Beckman Coulter AMPURE XP	Fisher Scientific	Cat# NC9959336
EasySep Human T Cell Isolation Kit	Stem Cell Technologies	Cat# 17951
Dynabeads Human T-Activator CD3/CD28	ThermoFisher	Cat# 11161D
Deposited Data		
scRNA-seq data	This paper	GEO: GSE117131
RNA-seq data	This paper	GEO: GSE117129
Experimental Models: Cell Lines		
B16-F10 mouse Melanoma cell line	ATCC	Cat# CRL-6475
143B human Osteosarcoma cell line	ATCC	Cat# CRL-8303
Experimental Models: Organisms/Strains		
Mouse: C57BL/6J	The Jackson Laboratory	Stock No: 000664
Mouse: B6.SJL-Ptprc^{a} Pepc^{b}/BoyJ	The Jackson Laboratory	Stock No: 002014
Mouse: NOD.Cg-Prkdc^{scid} Il2rg^{tm1Wjl}Tg(CMV-IL3,CSF2,KITLG)1Eav/MloySzJ	The Jackson Laboratory	Stock No: 013062
Software and Algorithms		
Bead-based Normalizer	Finck et al., 2013	https://med.virginia.edu/flow-cytometry-facility/wp-content/uploads/sites/170/2015/10/3_Finck-Rachel_CUGM_May2013.pdf
Cytobank	Cytobank	https://www.cytobank.org/
t-SNE	van der Maaten and Hinton, 2008	https://cran.r-project.org/web/packages/Rtsne/index.html
PhenoGraph	Levine et al., 2015	https://doi.org/10.1016/j.cell.2015.05.047
Cytofkit v1.r.0	Chen et al., 2016	https://bioconductor.org/packages/release/bioc/html/cytofkit.html
FlowJo (version 10.1r5)	TreeStar	http://flowjo.com/
Seurat (version 1.4)	Rizzo, 2016; Satija et al., 2015	https://satijalab.org/seurat/
FeatureCount R package v1.22.2	Liao et al., 2013	https://rdrr.io/bioc/Rsubread/man/featureCounts.html
RSubread R package v1.30.5	Liao et al., 2013	http://bioconductor.org/packages/release/bioc/html/Rsubread.html
edgeR v3.22.3	Robinson et al., 2010	https://bioconductor.org/packages/release/bioc/html/edgeR.html

(*Continued on next page*)

Continued

REAGENT or RESOURCE	SOURCE	IDENTIFIER
ZEN	ZEISS	https://www.zeiss.com/microscopy/int/products/microscope-software/zen.html
HyVolution 2	Leica	https://www.leica-microsystems.com/products/confocal-microscopes/details/product/hyvolution-2/downloads/
Image-Pro Premier	Media Cybernetics	http://www.mediacy.com/imagepro
Huygens Essential	Scientific Volume Imaging	https://svi.nl/HuygensSoftware
Imaris	Bitplane	http://www.bitplane.com/imaris/imaris
GraphPad Prism 7	GraphPad Software	http://www.graphpad.com

CONTACT FOR REAGENT AND RESOURCE SHARING

Further information and requests for reagents may be directed to and will be fulfilled by lead contact Catherine C. Hedrick (hedrick@lji.org).

EXPERIMENTAL MODEL AND SUBJECT DETAILS

Mice

C57BL/6J, B6 CD45.1 congenic mice, and NSG-SGM3 mice were purchased from The Jackson Laboratory. Mice were fed a standard rodent chow diet and were housed in microisolator cages in a pathogen-free facility. Mice were euthanized by CO_2 inhalation followed by cervical dislocation. All experiments followed approved guidelines of the La Jolla Institute for Allergy and Immunology Animal Care and Use Committee, and approval for use of rodents was obtained from the La Jolla Institute for Allergy and Immunology according to criteria outlined in the Guide for the Care and Use of Laboratory Animals from the National Institutes of Health. Animals were randomly assigned to groups from available mice bred in our facility or ordered from distributor. Experiments in this study used male animals 6-10 weeks of age in good health. If animals were observed with non-experiment related health conditions (i.e., malocclusion, injuries from fighting, etc.), animals were removed from study groups. For tumor studies, B16F10 melanoma cells and 143B human osteosarcoma cells were obtained from ATCC. Cell lines were tested for being pathogen free. Cell lines were maintained in DMEM medium containing 10% heat-inactivated FBS, 2 mmol/L l-glutamine, 1 mmol/L sodium pyruvate, 50 U/mL penicillin, 50 μg/mL streptomycin. For tumor injection, the hair around the tumor injection area of the 6-10 week old mice or adoptive transfer recipients was removed before injection. For Figure 4A and S5A, 5×10^5 B16F10 cells were washed and resuspended in 100 ul D-PBS and then SubQ injected into the rear flank of the mouse, and the tumor-bearing mice were euthanized by CO_2 inhalation followed by cervical dislocation at Day 14 post-tumor injection. For Figure 4B and S5B, 3×10^5 B16F10 cells were washed and resuspended in 100 ul DPBS and then SubQ injected into the rear flank of the mouse, and the tumor size were measured with a digital caliper at Day 12 and Day 22 post-tumor injection. For Figures 7B and 1×10^6 143B human osteosarcoma cells were washed and resuspended in 100 ul DPBS and then SubQ injected into the rear flank of the mouse, and the tumor size were measured with a digital caliper at Day 10 post-tumor injection. Tumor volume was calculated using the formula V (volume) = $D \times d^2/2$ (D is the largest measured tumor diameter and d is the smallest measured tumor diameter). Laboratory personnel were blinded to the identities of experimental groups during sample collection and analysis.

Human BM cells

Fresh BM samples of anonymous healthy adult donors were obtained from AllCells, Inc. (Alameda, CA). The cells were stained for either flow cytometry or FACS-sorting following protocols described in the Flow Cytometry and Cell Sorting section.

Melanoma Patient Blood Collection

Blood from melanoma patients (no previous radiation, no prior chemo treatment) was collected in EDTA-tubes by the Biospecimen Repository Core Facility (BRCF) at University of Kansas Cancer Center and delivered via overnight shipping. In the meantime, blood from healthy donors were collected in EDTA-tubes in La Jolla Institute for Allergy and Immunology and stored and treated similarly as control groups for the study. All blood samples were processed at the same time and cells were stained for flow cytometry followed by the protocol described in the Flow Cytometry and Cell Sorting section.

Human Peripheral Blood Collection

EDTA-coated blood from healthy volunteers was obtained after written informed consent under the guidelines of the Institutional Review Board of the La Jolla Institute for Allergy and Immunology and in accordance with US Department of Health and Human Services

Policy for protection of Human Research Subjects (VD-057-0217). Cells were stained for flow cytometry followed by the protocol described in the Flow Cytometry and Cell Sorting section.

METHOD DETAILS

Cell suspension for mass cytometry and flow cytometry

BM cells were harvested from femurs, and tibias of 6-10 week old mice. Bones were centrifuged for the collection of marrow. For the adoptive transfer experiments, donor BM cells were collected and stained under sterile conditions. Peripheral blood was obtained by cardiac puncture with an EDTA-coated syringe. For Figure 6B and S6B, a drop of blood was obtained from the saphenous vein of the adoptive transferred NSG-SGM3 mice recipients. All samples (both mouse and human) were collected in ice cold D-PBS (GIBCO) with 2 mM EDTA to prevent cation-dependent cell-cell adhesion. Prior to staining cells, cells were subject to a red blood cell lysis (RBC lysis buffer, eBiosciences) at room temperature (5 min x 1 for BM cells, 10 min x 2 for blood cells). Cells were washed and filtered through a 70 μm strainer. Cell suspensions were prepared by sieving and gentle pipetting to reach final concentration of 3×10^6 cells per 100 ul buffer.

Mass Cytometry Antibodies

Metal-conjugated antibodies were purchased directly from Fluidigm for available targets. For all other targets, purified antibodies were purchased from the companies listed in Table S1. Antibody conjugations were prepared using the Maxpar Antibody Labeling Kit according to the recommended protocol provided by Fluidigm. Maxpar-conjugated antibodies were stored in PBS-based antibody stabilization solution (Candor Biosciences) supplemented with 0.05% NaN3 at 4°C. All antibodies were titrated before use.

Mass Cytometry (CyTOF)

For viability staining, cells were washed in PBS and stained with Cisplatin (Fluidigm) to a final concentration of 5 μM. Prior to surface staining, anti-CD16/32 (151Eu) antibody was added to cell suspension in ice-cold staining buffer (PBS + 2mM EDTA + 0.1% BSA + 0.05% NaN3) to stain and block the Fc receptors for 15 min. The surface antibody cocktail listed in Table S1 was then added into the cell suspension for 1h. The cells were then washed and fixed with 2% paraformaldehyde overnight at 4°C. After fixation, cells were washed in staining buffer and permeabilized using Foxp3/Transcription Factor Staining Buffer (eBioscience) for intracellular staining according to the manufacturer's protocol. Following permeabilization, cells were washed twice with 1 mL 1X Perm Buffer (Saponin-based). The intracellular antibody cocktail listed in Table S1 were added into cell suspension for 1h. Cells were then washed in staining buffer and stained with DNA intercalator (Fluidigm) containing natural abundance Iridium (191Ir and 193Ir) prepared to a final concentration of 125 nM in 2% paraformaldehyde. Cells were washed in staining buffer, with subsequent washes in Milli-Q water (EMD Millipore) to remove buffer salts. Cells were resuspended in Milli-Q water with a 1:10 dilution of EQ Four Element Calibration beads (Fluidigm) and filtered through a 35 μm nylon mesh filter cap (Corning, Falcon). Samples were analyzed on a Helios 2 CyTOF Mass Cytometer (Fluidigm) equipped with a Super Sampler (Victorian Airship & Scientific Apparatus) at an event rate of 500 events/second or less. Mass cytometry data files were normalized using the bead-based Normalizer (Finck et al. 2013) and analyzed using Cytobank analysis software (https://www.cytobank.org/). The PhenoGraph clustering (Levine et al., 2015) and isomap dimensionality reduction were done using R package cytofkit (Chen et al., 2016). Hierarchical clustering was used to determine two meta-clusters based on the median of markers' expression from each PhenoGraph clusters.

Flow Cytometry and Cell Sorting

All mouse FACS staining was performed in FACS buffer (D-PBS + 1% BSA + 0.1% sodium azide + 2mM EDTA) on ice. All human FACS staining was performed in FACS buffer (D-PBS + 1% human serum + 0.1% sodium azide + 2mM EDTA) on ice. Cells were filtered through sterile 70 μm cell strainers to obtain a single cell suspension (30,000 cells per μl for flow cytometry analysis, 0.5 - 2 × 107 per ml for sorting). Prior to surface staining, anti-CD16/32 (FITC) antibody (for mouse) or human Fc receptors blocking reagent (MACS Miltenyi Biotec) was added for 15 min to stain and block the Fc receptors. Surface staining was performed for 30 minutes in a final volume of 500ul for FACS sorts and 100ul for regular flow cytometry. Cells were washed twice in at least 200ul FACS buffer before acquisition. Cells were sorted using a FACS Aria II and Aria-Fusion (BD biosciences) and conventional flow cytometry using an LSRII or a LSR Fortessa (BD Biosciences). All flow cytometry was performed on live cells. Calculations of percentages of $CD45^+$ immune cells were based on live cells as determined by forward and side scatter and viability analysis. All analyses and sorts were repeated at least 3 times, and purity of sorted fractions was checked visually and by FACS reanalysis of the surface markers. Data were analyzed using Cytobank (https://www.cytobank.org/) and FlowJo (version 10.1r5).

Confocal Microscopy

Cells were FACS-sorted by using the flow cytometry panel shown in Figure S3D and resuspended in PBS. Following fixation in 4% methanol-free formaldehyde in PBS for 10 min at room temperature, cells were washed with PBS and resuspended in 5% normal donkey serum, 0.3% Triton X-100 in PBS for one hour. Cells were then incubated with a rabbit anti-Ki67 monoclonal antibody (clone SP6, Abcam, 1:150) or negative control (normal rabbit IgG) in 1% bovine serum albumin and 0.3% Triton X-100 in PBS overnight at 4°C. Cells were washed twice with PBS and incubated with anti-rabbit IgG (H+L) F(ab')2 fragment conjugated to Alexa Fluor

647 (Cell Signaling, #4414, 1:500) and Hoechst (1:1000 of 10 mg/ml solution) for one hour at room temperature. After washing, cells were adhered to poly-L-lysine coated #1.5H coverslips and embedded in Prolong Gold (Thermo Fisher). Samples were imaged with a Zeiss LSM780 and Leica SP8 confocal microscopes using a 63x/1.40 NA oil-immersion objectives. Images were processed with ZEN or Leica HyVolution software and 3D reconstructions of DNA were created in Imaris software. The mean and integrated fluorescence intensity (select the one you will show) of Ki-67 within the nuclear regions were calculated in Image-Pro Premier. To reduce Z-stretching confocal images were deconvolved with Huygens Essential. Analysis of the surface area, volume and sphericity was performed in Imaris software.

Adoptive transfer

Recipient mice were housed in a barrier facility under pathogen-free conditions before and after adoptive transfer. NSG-SGM3 recipient mice were maintained in sterile conditions at all times. CD45.1 recipient mice were fed with autoclaved acidified water with antibiotics (trimethoprimsulfamethoxazole) for 3 days before the adoptive transfer. Sub-lethally irradiated recipient mice received 600 Rads. Donor BM cells were collected and FACS sorted as described in the flow cytometry section. Mouse and human progenitor cells were sorted directly into sterile FBS and kept chilled during sorting. Cells then were washed and resuspended in ice-cold D-PBS for injection. 50,000 donor progenitors in 200 ul DPBS were delivered into each recipient mouse for Figures 3 and 4. 25,000 donor progenitors in 200 ul DPBS were delivered into each recipient mouse for Figures 6 and 7. All adoptive transfer experiments were achieved via tail vein injection. After the adoptive transfer, recipient mice were provided with autoclaved food and autoclaved acidified water with antibiotics.

In vitro progenitor differentiation assay

Sorted progenitor cells were seeded into 6-well plates and cultured for 10 days with MethocultTM GF M3434 media (Stem Cell Technologies) according to the manufacturer's protocol. The numbers of wells containing proliferated colonies were counted for -colony-forming assays.

Human T cell co-culture with NePs

To investigate the effects of NeP subsets on human autologous T cell activation, CD3+ T cells were negatively-selected from healthy donor PBMCs (LJI NBDP) according to manufacturer's instructions (Stem Cell Technologies). CD34+ hNeP, CD34- hNeP, and mature neutrophils were FACS sorted from fresh human BM obtained from AllCells, Inc. (Alameda, CA). The sorted CD3+ T cells were cultured with CD34+ hNeP, CD34- hNeP, and mature neutrophils at a 2:1 ratio, in the presence or absence of 2μg/mL plate-bound anti-CD3 Ab (Biolegend) for 24 hr at 37°C with 5% CO2. For polyclonal stimulation, purified CD3+ T cells were incubated with anti-CD3,-CD28 Dynabeads (Invitrogen). To investigate CD69 activation, cells were collected and stained with anti-human CD3, CD69, and a fixable live/dead viability dye at 24 hours post stimulation. 75,000 events were collected on the Fortessa (BD Biosciences), and data was analyzed using FlowJo (v.10.3).

Single-cell RNA-seq. 3′ end

Mouse Cluster#C cells were FACS-sorted using the flow cytometry panel shown in Figure S2C. Human hNeP were FACS-sorted by using the flow cytometry panel shown in Figure 5A. Single cell RNA-Sequencing was performed using Chromium Single Cell 3′ v2 Reagent Kits (10x Genomics) following the manufacturer's protocol (Zheng et al., 2017). Briefly, after sort collection, cells were resuspended in PBS at concentration ranging between 400 to 600 cells per μl. Between 5,000 to 10,000 cells were loaded for gel bead-in-emulsion generation and barcoding. To increase barcode diversity, samples were split in 2 technical replicates for all downstream steps: Reverse transcription, cDNA amplification, fragmentation and library preparation. Final libraries with size ranging between 200 to 1000 bp were size-selected using Ampure XP beads (Beckman Coulter). Quality and quantity of samples was controlled at multiple steps during the procedure by running small fraction (< 5%) of sample on BioAnalyzer (high sensitivity DNA chip, Agilent). Libraries were sequenced on HiSeq2500 platform to obtain 26 (read1) x 100 (read2) paired-end reads.

Single cell RNA-Seq analysis

Using Cell Ranger v1.3.0 (10x genomics), reads were aligned on the mm10 reference genome for mouse and hg19 reference genome for human and unique molecular identifier gene expression profiles were generated for every single cell reaching standard sequencing quality threshold (default parameters). On average we obtained data for 2868 cells for mouse samples and 518 cells for human samples, and on average 46,477 reads per cell for mouse and 274,080 reads per cell for human. Only confidently mapped, non-PCR duplicates with valid barcodes and UMIs were used to generate a gene-barcode matrix for further analysis. Counts were normalized to get counts per million (CPM). Unbiased clustering of single cells was performed using Seurat (version 1.4) (Rizzo, 2016; Satija et al., 2015). Principal Component Analysis (PCA) was performed using a set of top variable genes (ranging between 647 to 2142 genes) and then dimensionality reduction was performed using t-SNE algorithm with top 10 to 18 PCAs. For Figure 2A, tSNE 2D plots were obtained applying Seurat scRNA-Seq analysis R Package (using 12 first PCA, and 810 most variable genes with resolution parameter set at 0.03).

RNA-Seq

Cells were FACS-sorted by using the flow cytometry panel shown in Figure S3D. RNA-Seq was prepared on FACS sorted BM cells using Universal Plus mRNA-Seq (Nugen) and sequenced on an Illumina 2500 instrument. Single-ended reads in FASTQ format were mapped to mouse genome (mm10) using Rsubread (Liao et al., 2013) and overlapped with UCSC mm10 transcriptome annotation from using FeatureCount R package(Liao et al., 2014). Gene expression level was then quantified as counts per million (CPM) using edgeR(Robinson et al., 2010).

QUANTIFICATION AND STATISTICAL ANALYSIS

Data for all experiments were analyzed with Prism software (GraphPad). For Figure 4A and S5A, unpaired t tests were used to compare the values in tumor groups to healthy groups. P value was calculated based on two-tailed comparison with 99% confidence level. For Figure 4B and 7B, unpaired ordinary one-way ANOVA was used for multiple comparisons between experimental groups and the control group. P value was calculated based on Dunnett's test with 95% confidence level. No statistical methods were used to predetermine sample size. No animal or sample was excluded from the analysis.